
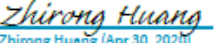






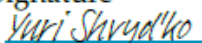
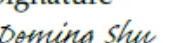



CBXFEL PHYSICS REQUIREMENTS DOCUMENT FOR THE
OPTICAL CAVITY BASED X-RAY FREE ELECTRON LASERS
RESEARCH AND DEVELOPMENT PROJECT

April 16, 2020

CBXFEL project PRD Document Approval

Gabriel Marcus	 <u>Gabriel Marcus (Apr 30, 2020)</u>	
	Signature	Date
Zhirong Huang	 <u>Zhirong Huang (Apr 30, 2020)</u>	
	Signature	Date
Diling Zhu		
	Signature	Date
Tien Fak Tan	 <u>Tien Tan (Apr 30, 2020)</u>	
	Signature	Date
Harmanpreet Bassan	 <u>Harmanpreet Bassan (Apr 30, 2020)</u>	
	Signature	Date
Georg Gassner		
	Signature	Date
Ryan Lindberg		
	Signature	Date
Kwang-Je Kim	 <u>Kwang-Je Kim (Apr 30, 2020)</u>	
	Signature	Date
Yuri Shvyd'ko	 <u>Yuri Shvyd'ko (Apr 30, 2020)</u>	
	Signature	Date
Deming Shu	 <u>Deming Shu (Apr 30, 2020)</u>	
	Signature	Date
Marion White	 <u>Marion M. White (Apr 30, 2020)</u>	
	Signature	Date

Contents

1	Purpose	5
2	Scope	6
3	Definitions	7
4	Responsibilities	8
4.1	Electron beam	8
4.2	Chicanes	8
4.3	Undulator	8
4.4	X-ray cavity optics and diagnostics systems	8
4.5	Systems installation, integration and operation	9
5	Overview	10
6	General Requirements	13
6.1	Electron Beam	13
6.1.1	Single bunch	13
6.1.1.1	XRAFEL	13
6.1.1.2	XFELO	14
6.1.2	Double-bunch production	14
6.1.2.1	General Requirement	14
6.1.2.2	XRAFEL	14
6.1.2.3	XFELO	15
6.1.3	Double bunch operational considerations	16
6.1.3.1	Injector lasers	16
6.1.3.2	RF	17
6.1.3.3	Transverse Kickers	17
6.1.4	Diagnostics	18
6.2	Four-Dipole Chicanes	18
6.2.1	Chicane Dipole Magnets	19
6.2.1.1	Magnet Heat Load in Undulator Tunnel	20
6.2.1.2	Magnet Alignment and Field Quality Tolerances	20

6.2.1.3	Prescribed Horizontal Alignment Offsets	20
6.2.1.4	Power Supply Performance Requirements	21
6.3	Undulator System	21
6.4	X-ray Cavity System	23
6.4.1	Cavity system layout and components	23
6.4.2	Precision and Stability requirements	24
6.4.2.1	XRAFEL tolerances	26
6.4.2.2	XFELo tolerances	27
6.4.3	X-ray optics elements	28
6.4.3.1	Diamond crystal optics: specification, characterization, and machin- ing	28
6.4.3.2	Crystal temperature stability	29
6.4.3.3	Focusing optics	30
6.4.3.4	Intracavity beam sampling optics	30
6.4.4	Cavity out-coupling mechanisms	31
6.4.4.1	Thin diamond crystal	31
6.4.4.2	Diamond transmission grating	33
6.4.5	X-ray Diagnostics	33
6.4.5.1	X-ray intensity diagnostics	34
6.4.5.2	X-ray position and profile diagnostics	35
6.4.5.3	Spectral diagnostics	36
6.4.6	Cavity Alignment Procedure	38
6.4.7	Mechanical System	40
6.4.7.1	Laser Interferometer	41
6.4.7.2	Capacitive Sensor	42
6.4.7.3	Vacuum System	42
6.4.7.4	Metrology Reference frame and Base	42
6.4.7.5	Nanopositioning Stages for X-ray Optics and XBPMs Motion Control	43
6.5	Electron/photon Beam Overlap Diagnostics	46
6.5.1	Transverse overlap	46
6.5.2	Longitudinal overlap	46
6.6	Measurements	47
6.6.1	Ring-down	47
6.6.1.1	Intra-cavity measurement	47
6.6.1.2	Extra-cavity measurement	48
6.6.2	Two pass gain	48
6.6.2.1	XRAFEL	48
6.6.2.2	XFELo	48
6.7	Controls	49
6.8	Machine Protection Systems	50
6.9	Other global and safety requirements	50

7 End Notes	52
Bibliography	53

Chapter 1

Purpose

This document describes the physics requirements for the Optical Cavity Based X-ray Free Electron Lasers (CBXFEL) research and development project.

Chapter 2

Scope

Cavity based XFEL systems have the following subsystems and components that will be described in this document:

1. Electron bunches (single and two-bunch)
2. Chicanes
3. Undulator
4. X-ray Cavity
5. Diagnostics

The requirements for the high-gain (XRAFEL) and low-gain (XFELO) FEL systems will be broken out where appropriate. All infrastructure will be installed on the LCLS-II hard X-ray (HXR) undulator beamline.

Chapter 3

Definitions

ANL	Argonne National Laboratory
CBXFEL	Cavity-based X-ray free electron laser
CRL	Compound refractive lens
FEL	Free electron laser
MPS	Machine protection system
SASE	Self-amplified spontaneous emission
SLAC	SLAC National Accelerator Laboratory
XFELO	X-ray FEL Oscillator
XRAFEL	X-ray Regenerative Amplifier FEL
HXR	Hard X-ray
RF linac	Radio frequency linear particle accelerator
BC1	First bunch compressor
BC2	Second bunch compressor
SLED	SLAC energy doubler
BPM	Beam position monitor

Chapter 4

Responsibilities

This chapter defines at a high level the various sub-system leads, roles, and highlights important project interfaces. We emphasize that the design of the overall system and each subsystem will be a highly collaborative joint effort.

4.1 Electron beam

1. Requirement and specification for XFELO: ANL
2. Requirement and specification for XRAFEL: SLAC
3. Electron beam preparation/characterization/delivery/diagnostics: SLAC

4.2 Chicanes

1. Requirement and specification of optical enclosures: ANL
2. Requirement and specification of magnetic chicane: SLAC
3. Chicane fabrication and installation: SLAC

4.3 Undulator

1. All modifications: SLAC

4.4 X-ray cavity optics and diagnostics systems

1. Diamond crystals acquisition and screening: RIKEN SPring8 Center
2. Diamond crystal optics design, machining, mounting, and characterisation: ANL
3. Be paraboloidal lenses acquisition and characterisation: ANL
4. Cavity mechanical system and motion control: design/build/test by ANL at the individual component level including EPICS driver interfaces. SLAC responsible for system level integration, high level application, and user interface.

5. Cavity components initial alignment/metrology: ANL
6. Cavity alignment diagnostics: design/build/functional-test by ANL. SLAC responsible for installation, controls and readout integration, and user interfaces.
7. Intracavity diagnostics: SLAC
8. Beam overlap diagnostics: SLAC
9. Extra-cavity diagnostics: design/built/test by ANL. SLAC will be responsible for integration into experimental hutch control/data acquisition system and operation.
10. Cavity installation: SLAC

Subsystem commissioning and qualification will follow the responsibilities assigned as above. All ANL responsible subsystems will be delivered to SLAC by ANL (or arranged by ANL). As a part of the cavity installation activity, the subsystem's motion, power and feedback controls will be integrated with SLAC LCLS-II electrical hardware and software interfaces by SLAC. ANL and SLAC will lead the experimental program from XFEL and XRFEL respectively with common technical challenges being addressed jointly.

4.5 Systems installation, integration and operation

1. Interface control: ANL and SLAC

Agreements for the exact deliverables will be mutually agreed upon between subsystem and system integration at the start of the Preliminary Design phase. As a project goal, all subsystems listed above will be delivered with integrated motion, power and feedback controls, designed and tested to be fully functional with LCLS-II electrical hardware and software interfaces. Additionally, all subsystems should have documentation that will provide instructions for installation and integration. These efforts will minimize rework and keep installation on schedule.

2. Installation: SLAC
3. Systems controls and software integration: SLAC
4. Systems commissioning and operations: ANL and SLAC

Chapter 5

Overview

LCLS and the LCLS-II upgrade will primarily produce X-ray radiation through the process of self-amplified spontaneous emission (SASE). This mode of operation produces high-brightness X-ray pulses that are transversely but not longitudinally coherent. One solution for producing longitudinally-coherent FEL pulses is to store and circulate the output of an amplifier in an X-ray cavity so that the X-ray pulse can interact with the following fresh electron bunches over many passes. The X-ray cavity is formed by a set of narrow-bandwidth diamond Bragg crystals that provide both high reflectivity and monochromatization functionality. Seeding fresh electron bunches in this way, with sufficiently narrow bandwidth radiation and at powers well above the effective electron bunch shot-noise level, has many distinct advantages over traditional self-seeding concepts for the production of high-brightness and longitudinally coherent X-ray pulses. The LCLS-II upgrade will be capable of steady-state operation with repetition rates as high as 1 MHz, making the overall footprint of the X-ray optical cavity realistic.

The Optical Cavity Based X-ray Free Electron Laser project is a joint Argonne National Laboratory, SLAC National Accelerator Laboratory, and RIKEN SPring-8 collaboration aimed at studying the physics of cavity based FEL schemes and enabling their future implementation at high-repetition-rate facilities. In particular, crucial aspects of both the high-gain X-ray regenerative amplifier FEL (XRAFEL) and the X-ray FEL oscillator (XFEL) schemes will be studied and their performances demonstrated in a rectangular X-ray cavity that will be installed around the first seven LCLS-II hard X-ray undulator modules using two bunches delivered by the SLAC copper RF linac (see Figure 5.1a). The choice of a rectangular cavity geometry, rather than a tunable zig-zag (or bow-tie) geometry, is driven by the limitation of its transverse extent (see Figure 5.1b). Two-pass gain measurements as well as cavity ring-down measurements for both the high- and low-gain schemes will be performed.

The rectangular X-ray cavity will consist of four diamond crystals. The first two of these crystals reflect the X-ray pulse into and out of the undulator line, and will be located within 4-dipole electron bunch-delay chicanes that bracket the 7 undulator sections. Two additional crystals reflect the X-ray pulse back to the electron path in the undulator.

Four diamond crystals and two x-ray lenses on motion stacks form the basis of the optical cavity. These stacks will include nanoradian-level-resolution positioning stages with high-quality diamond optical components that are mounted in strain-free holders. The diamonds deployed in this cavity will be cut parallel to the (100) crystal surface. Two-pass gain measurements will be performed for both the low and high gain case using the C(400)* reflection planes at a 45° Bragg angle. The cavity geometry and reflection plane set the nominal photon energy and electron beam energy for the experiments. The main undulator and cavity parameters can be found in Table 5.1 while the main electron bunch parameters can be found in Table 5.2.

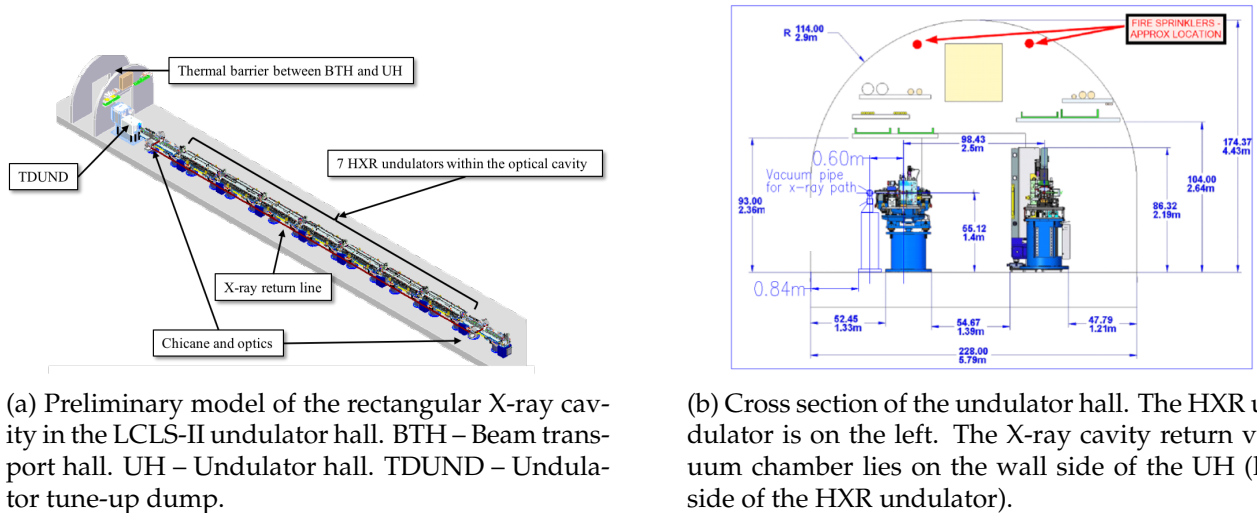


Figure 5.1: Layout in the undulator hall.

Parameter	Value	Unit
Undulator		
Period	2.6	cm
Periods per segment	130	-
Magnetic length per segment	3.4	m
Break length	0.612667	m
Number of segments	7	-
Total magnetic length	23.8	m
Total length	28.089	m
K	2.44	-
Cavity		
Crystal material	C*(400)	-
Bragg angle	45	degree
Photon energy	9.831	keV
Wavelength	1.26	Angstrom
Bragg reflection width (energy)	75	meV
Bragg reflection width (angle)	8	μ rad
Cavity roundtrip length	~ 65.3	m

Table 5.1: Main undulator and cavity parameters.

Parameter	XFELO	XRAFEL	Unit
Energy	10.3		GeV
Charge	100	150	pC
FWHM length	300	50	fs
RMS beam size	22	24	μ m
RMS angular divergence	1.1	1.2	μ rad
Two-bunch spacing	~ 65.3 (220)		m (ns)
Repetition rate	120		Hz

Table 5.2: Main electron bunch parameters.

The 4-dipole chicanes can be switched off and the optics extracted from the undulator line for normal SASE operation. In this case, the electron beam and x-rays proceed through the undulator unaffected. Switching between SASE and CBXFEL modes should be possible in a few minutes time. Trim magnets on each of the chicane dipole magnets will ensure that the relative phase between the electrons and x-rays is correct when operating in SASE mode (although this is not necessary for the upstream chicane).

The following sections detail the physics requirements of the various subsystems (both cavity and electron bunch) needed to ensure the measurements of the cavity ringdown and 2-pass gain for the low- and high-gain scenarios.

Chapter 6

General Requirements

6.1 Electron Beam

The electron beam specifications are driven by the desire to produce measurable FEL gain. This leads to requirements both on the single bunch quality and on tolerances in terms of trajectory, timing, and energy of the two bunches. In what follows we will specify the requirements for both the XFEL and XRFEL conditions whose parameters are outlined in Table 5.2. These two parameter sets should be considered as the particular low- and high-gain cases that we will target, but in practice some intermediate medium-gain configuration may be also be explored.

6.1.1 Single bunch

Single-bunch requirements pertain to both the leading and trailing electron bunches, and are driven by the desire for the trailing bunch to produce measurable FEL gain in a seeded interaction. To this end, both the XRFEL and XFEL configurations require a high-brightness electron beam that is consistent with the LCLS CuRF injector, compression, and transport. In particular, both require a beam of $\gtrsim 150$ pC at a mean energy of 10.3 GeV and with a normalized emittance $\varepsilon_{x,n} \lesssim 0.5$ mm-mrad. The nominal longitudinal properties in the high-gain XRFEL and low-gain XFEL differ as shown in Table 5.2, and we discuss these cases further in the next two subsections.

6.1.1.1 XRFEL

The electron beam for the XRFEL can adopt the routine machine setup that is typically used for hard x-ray SASE FEL operation. The injector starts with a bunch charge of 250 pC. The head and tail of the electron beam are truncated by a horizontal collimator in the middle of the first bunch compressor (BC1) to shape the longitudinal phase space and current profile. The bunch charge after BC1 collimation is set to be 150 pC, and the final beam current after the second bunch compressor (BC2) is about 3 kA. The BC2 energy is fixed at 5 GeV, and the downstream linac is configured to achieve a final energy of 10.3 GeV. Results from a start-to-end simulations based on this configuration are shown in Fig 6.1 and include the electron beam longitudinal phase space and current profile at the entrance of the HXR undulator. The simulated slice emittance is about 0.4 mm-mrad with a slice energy spread of about 1.5 MeV. This electron beam is capable of supporting sufficient single-pass and two-pass gain at the target photon energy of ~ 9.831 keV (see Section 6.6.2.1 for details), that in turn require reasonable cavity opto-mechanical tolerances (see Section 6.4.2.1 for details).

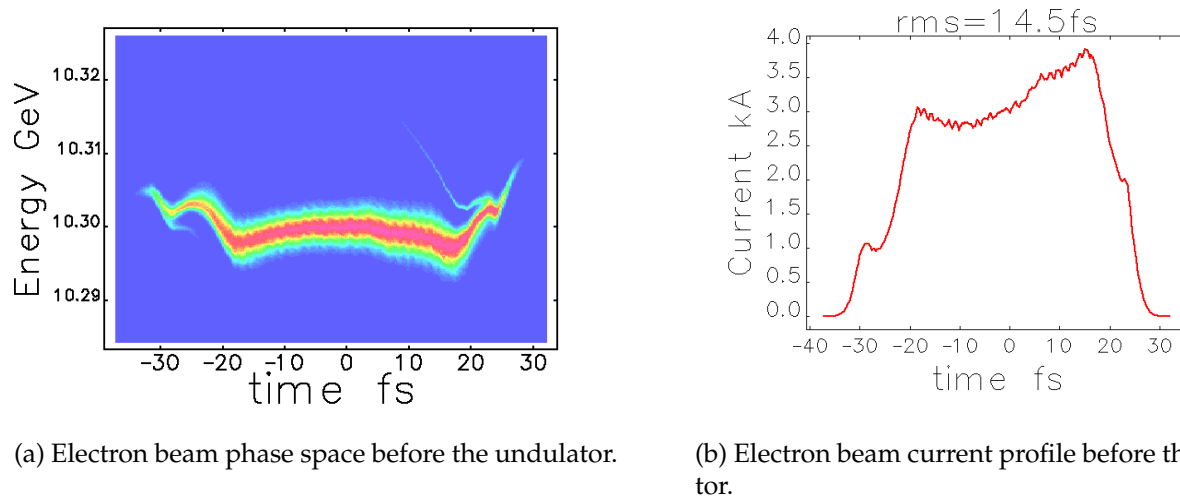


Figure 6.1: Simulated electron beam for XRAFEL test.

6.1.1.2 XFEL

The XFEL parameters are set to test a cavity-based FEL when the single-pass gain is the order of 1-5. For this, we require relatively modest longitudinal compression and commensurately lower energy spread. Specifically, the nominal XFEL design calls for a peak current of 333 A over a flat-top duration of 300 fs. Within this 300 fs the normalized energy spread should be $\sigma_\gamma/\gamma \lesssim 5 \times 10^{-5}$, while the projected energy spread should be $\lesssim 10^{-4}$ over the entire 300 fs window. These numbers are consistent with the LCLS experience that one typically gets an energy spread of 0.5 MeV per 1 kA peak current.

Start-to-end simulations have been performed, indicating that these parameters are achievable. Results of these simulations are shown in Figure 6.2. The electron beam at the entrance to the undulator has a peak current of 300 A over a flat-top duration of $\gtrsim 300$ fs. The overall projected energy spread is $\sim 5 \times 10^{-5}$ while the emittance and relative slice energy spread in the core are ~ 0.4 mm-mrad and $\sim 2 \times 10^{-5}$, respectively.

6.1.2 Double-bunch production

6.1.2.1 General Requirement

The primary goal of this experiment is to demonstrate that the x-ray pulse from a leading electron bunch, after propagating around the x-ray optical cavity, can be properly amplified by a trailing electron bunch. This leads to the requirement that the two electron bunches should have the same trajectory to within a fraction of the transverse electron beam size, the same energy at the level of the rms energy spread, and a temporal separation that matches the x-ray cavity round-trip time to within a fraction of the bunch length. We specify the nominal XRAFEL and XFEL requirements more precisely in the following two sections.

6.1.2.2 XRAFEL

The XRAFEL benefits from gain-guiding in the high-gain regime to relax the spatio-angular alignment tolerances between the returned x-ray pulse and the trailing electron bunch. To this end, the

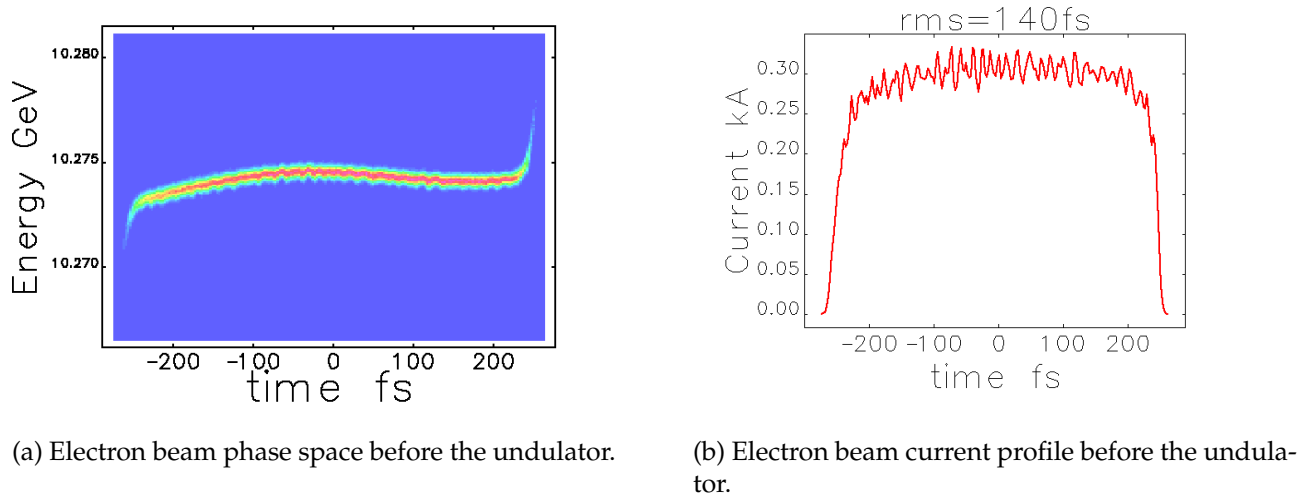


Figure 6.2: Simulated electron beam for XFEL test.

two electron bunches should nominally be aligned to the same trajectory to within $\sim 10 \mu\text{m}$ over a distance of $\sim 10 \text{ m}$. These tolerances should provide sufficient overlap between the returned x-ray pulse, assuming an aligned cavity, and the second electron bunch for a few gain lengths (the lethargy region in a seeded interaction). Tolerances will be moderated somewhat because the returned radiation mode size at the entrance of the undulator is larger than the waist size in the middle of the undulator.

The RMS temporal jitter between the two electron bunches should be held to less than 25 fs so that at least 68% of the shots will seed with at least 50% overlap between the returned x-ray pulse and the trailing electron bunch.

The mean energy difference between the two electron bunches should be held to less than half of the relative FEL bandwidth, $\rho^{3D} \sim 5 \times 10^{-4}$. Setting the mean energy difference tolerance to $\rho^{3D}/4$ means the relative mean energy difference should be held to less than 1.25×10^{-4} . The RMS jitter in the mean energy difference should be held to less than $\sim \rho^{3D}/10 \simeq 5 \times 10^{-5}$.

6.1.2.3 XFEL

The XFEL targets low gain with a relatively long electron bunch, and therefore typically has tighter trajectory but looser timing requirements than does the XRFEL. Figure 6.3(a) shows how the photon output within the crystal bandwidth changes as we vary the initial displacement Δx between the two electron bunches, where the red and blue lines assume two different commercially-available CRL focal lengths, $f = 14.18 \text{ m}$ and $f = 28.36 \text{ m}$, respectively. The plot indicates that trajectory offsets larger than ~ 10 microns reduce the FEL output, while requiring the two bunches to be held within $\lesssim 4$ microns transversely results in good overlap between the spontaneous emission and the trailing electron bunch, and a negligible reduction in FEL gain. Each point in Fig. 6.3(a) is obtained from the average of 20 statistically-independent simulations using the 3D FEL code *genesis*.

The longitudinal tolerances can be estimated as follows. We expect that keeping the longitudinal overlap to less than 10% of the bunch length will result in minimal reduction of the FEL gain, while the energy difference between the two bunches should be maintained to a small fraction of the low-gain FEL bandwidth $1/2N_u \sim 5 \times 10^{-4}$. Figure 6.3(b)-(c) shows that these estimates are quite reasonable: timing variations of less than 30 fs negligibly impact FEL gain, while energy dif-

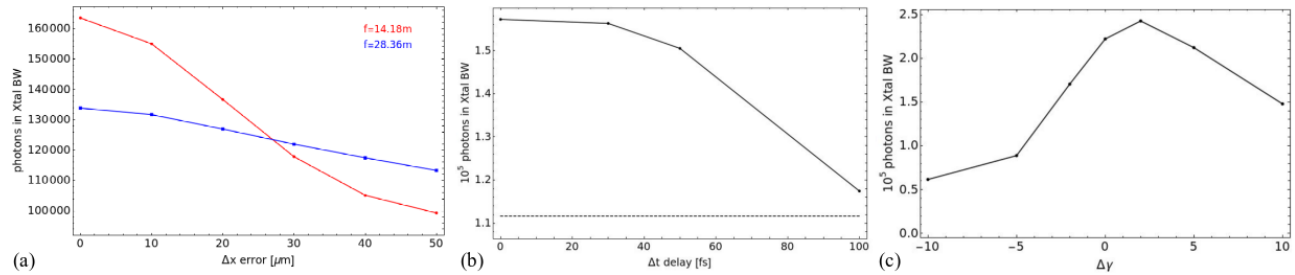


Figure 6.3: Two-bunch electron beam tolerances for the XFELO. (a) plot of the simulated photon output as a function of the displacement between the electron beams Δx for two different CRL focal lengths. (b) shows how the output depends upon the timing difference between the bunches. (c) plot of the output as a function of the energy difference between the bunches, which is essentially the FEL low-gain curve.

ferences between the two bunches of $\Delta\gamma \lesssim 1$ ($\Delta\gamma/\gamma \lesssim 5 \times 10^{-5}$) can also be tolerated. The plots in Figure 6.3(b)-(c) use $f \approx 13$ m, but the conclusions should be largely independent of f . Hence, we conclude that the timing jitter specifications for the XFELO are relaxed from that of the XRA FEL, while the energy jitter requirements are similar.

6.1.3 Double bunch operational considerations

There are many difficulties associated with establishing a robust double electron bunch mode of operation. The CBXFEL project will require two electron bunches, ideally with identical properties (current, energy spread, emittance, etc.), to enter the LCLS-II HXR undulator temporally separated by the x-ray cavity round trip time (see Table 5.1). The following sections address the key challenges associated with operating the LCLS injector, linac, and transport with two electron bunched separated by greater than 200 ns. Given the recent and significant interest in double and multi-bunch operation, a dedicated effort is underway within the LCLS Operations group to streamline and optimize this mode of operation.

6.1.3.1 Injector lasers

The LCLS Laser Science and Technology division supports the injector laser system, which provides ultrashort pulses of UV light to produce ultrashort electron bunches from the Cu cathode in the injector. The injector laser system is redundant by design and is composed of two identical Ti:Sapphire systems. In typical single-bunch operation, only one laser is used at a time while the other laser acts as a hot swap spare. Double-bunch operation with large temporal separations, however, leverage both lasers simultaneously to generate two electron bunches off of the cathode. This will be the operational condition for the CBXFEL project, which has inherent in it a number of challenges. Non-uniformities and differences in the two laser profiles (position, pointing, and distribution) coupled with non-uniform cathode quantum efficiency can lead to the production of non-uniformities within a single electron bunch and, more importantly here, differences between the two generated electron bunches. A number of laser parameters can be controlled, some independently and some only simultaneously, to facilitate the production of two identical electron bunches in order to meet the requirements established above. These parameters include the control of each laser's position on the cathode (x, y, t), distinct second moments (σ_x, σ_y , pulse length), and pulse intensities. Similar controls are in place for both laser heaters. Successful double bunch FEL operation has been performed in the past with the existing injector/heater laser controls infrastructure for two-bunch

temporal spacings greater than 200 ns.

6.1.3.2 RF

The energies and bunch lengths of the two electron bunches can be influenced by the RF waveform in the accelerator sections. With a typical RF fill time of 825 ns and the desired bunch separation of about 220 ns the possible change is about 25%. Since we want to have as closely as possible the same beam parameters except their arrival time, the RF parameter should be as close as possible. For the RF systems of L0A, L0B, L1S, this is roughly achieved by providing a long, flat (un-SLEDED) waveform. The RF system of Gun and L1X have special waveform and hence require special treatment. For the rest of the Linac the SLEDED waveform is a challenge. The electron bunch sees an integrated accelerating voltage that is peaked in time. Single bunch operation is timed to be at the peak of the integrated accelerating voltage. For two-bunch operation, the peaked RF pulse can be delayed by about 110 ns so that the first bunch sits on the rising slope while the second bunch sits on the falling slope. This is easy in concept but is still quite challenging in practice. First, the RF timing system step is about 8.4 ns and is too large to balance the energies of two bunches. The resulting energy difference is about 0.05% for one 100 m long Linac sector. By reducing the number of klystrons from 8 to 2, we can reduce this energy difference to 0.013% per sector. Second, since the peaked RF waveform is mainly in the upstream (downstream) end of an accelerator section for the first (second) bunch, the two bunches will experience different transverse kicks and different chirps resulting in different bunch lengths. The longitudinal effect can be mitigated by modifying the RF waveform while the transverse effect needs to be mitigated by new transverse kickers (see Section 6.1.3.3).

The main reference oscillator RF frequency is 476,000,000.08 Hz, with an extremely-good stability of 0.1 Hz out of 476 MHz. A 1-Hz change corresponds to a 0.5-fs change over 220 ns. Such a phase stability does not yet guarantee that the two electron bunches will be at the same phase at the end of the linac with that precision due to the electron bunch compression. When an energy separation of 1.6% (80 MeV out of 5 GeV) between two bunches is introduced before the BC2 chicane with an R56 value of -28 mm, one bunch can be delayed relative to another bunch by 1.5 ps ($= 28 \text{ mm} * 0.016 / 105 \text{ mm} * 360$). This feature can be used to scan the bunch separation by about ± 1.5 ps. The energy difference has to be compensated in L3 for these two bunches. The shot-to-shot rms energy jitter is about 20 times smaller than 1.6% and the two bunch difference energy jitter is another factor of 4 lower resulting in a separation time jitter about 20 fs (rms).

6.1.3.3 Transverse Kickers

To overlap the trailing bunch perfectly with the X-ray pulse from the first bunch in the undulator we have to control x, x', y, y' of the second bunch. At short delays of less than 20 ns wakefields can be used, at different energies dispersion can be used, and small adjustments can be made moving the center of the laser spots differently inside the iris at the injector. The first two don't work for the CBXFEL due to the longer delay and the requirement of the exact same energies. So four kickers have to be used. A dedicated LCLS Accelerator Improvement Project (AIP) will provide and install four fast kickers to meet the needs of the CBXFEL project. It is foreseen to install two kickers (x and y) in the instrument sections in Sector 21 (21-9) at 1.7 GeV and two (x and y) roughly 60 degrees phase advance away in Sector 22 (22-9) at 3.2 GeV. The kicker structure will be about 0.5 m long with an inner diameter of 20 mm. The power supplies have to be bipolar. Details of kicker requirement for two-bunch operation can be found in a separate LCLS AIP PRD.

6.1.4 Diagnostics

The typical beam diagnostics either show a certain sum of the two bunches or they can distinguish between the two bunches and give two values per pulse. At 220 ns the BPMs (Beam Position Monitors) raw waveform signal shows two separated pulses that can be processed individually. However, slow detectors like toroids and peak current monitors typically see the sum of both bunches.

The longitudinal phase space distribution is separated by the X-band radio-frequency deflector (XTCAV) when it is not perfectly tuned. This allows us to measure for each bunch the energy and its distribution, the bunch length and its distribution and the correlation between the two on the downstream dump screen to the required precision.

6.2 Four-Dipole Chicanes

The CBXFEL system will contain two sets of four dipole magnets arranged to create a chicane in the path of the electron beam. The first chicane (called the *upstream* chicane) will be located in cell 13 of the HXR undulator beamline while the second chicane (called the *downstream* chicane) will be located in cell 21 of the HXR undulator beamline (see Figure 6.7). The primary purpose of both of these chicanes is to horizontally steer the electron beam around the optical cavity components and prevent the electron beam from getting too close to the diamond mirrors. The upstream and downstream chicanes, however, *may* have some differences, as detailed below.

The upstream and downstream chicanes will have the ability to operate in both the SASE and CBXFEL modes. During CBXFEL operation, the chicane main power supplies will be set to their nominal values and will bend the electron beam away from the diamond optics (toward the “aisle” of the undulator hall). The electron beam must maintain a minimum distance of 2.6 mm from the inserted optics to keep the diamond out of any surviving beam halo. After deflection, the electron beam must return to within a 100 nrad residual beam angle and a 5 micron residual beam offset with respect to the undeflected trajectory (after correction with downstream corrector magnets if necessary).

During SASE operation, the optical cavity diamond mirrors are retracted, and the chicanes are turned off. The phase shift across the downstream chicane break will need to be controlled by powering trim windings on each of the dipole magnets. The strength of the trim coils must be sufficient to correct the phase shift error when running normal SASE beams with the highest LCLS photon energy driven by the electron beam coming from the copper RF linac. While not required here, the upstream chicane should also have the capability to provide a phase shift to enable future operational flexibility (e.g., so that it can be moved at some later date to another location).

If at all possible, the downstream chicane should support two separate optics enclosures. The upstream enclosure would house the optics chamber for the CBXFEL project. The downstream enclosure would house the optics chamber for a separate project (Double-bunch XFEL). If, however, the CBXFEL project requires additional space for electron or photon beam diagnostics, the optics chamber can be housed in the downstream enclosure leaving the upstream enclosure free.

The chicane design that can accommodate both chambers will presumably look like the SXRSS chicane. The upstream chicane will house the CBXFEL optics chamber and can borrow the design either from the HXRSS or SXRSS systems. However, the SXRSS system is also the preferred choice here as the downstream enclosure can house a beam overlap diagnostic (see section 6.5). Table 6.1 lists the main parameters for the CBXFEL electron beam chicanes assuming the SXRSS design is adopted.

Parameter	Nominal	Minimum	Maximum	Unit
Electron beam delay	270	0	1500	fs
Delay precision at 1000 fs	0.2	0	1	fs
Electron beam displacement at chicane center	10.7	0	25	mm
Magnitude of residual beam angle	0	0	100	nrad
Magnitude of residual beam offset	0	0	5	μm

Table 6.1: Main upstream and downstream chicane parameters.

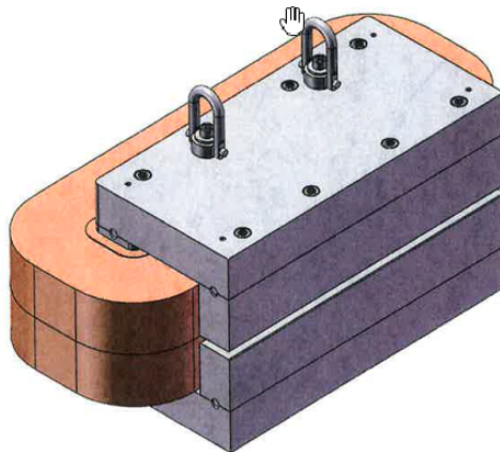


Figure 6.4: The XLEAP dipole magnet used for CBXFEL chicanes (main and trim coils shown).

6.2.1 Chicane Dipole Magnets

Each chicane's four dipole magnets are air-cooled, C-type rectangular electro-magnets and are identical to those used in the XLEAP experiment. The main coils of four magnets (per chicane) are powered in series by one main power supply, which is continuously adjustable from zero to full scale. Each of the four dipoles also include a $\pm 1\%$ trim coil (percent of max. main current), independently excited by bipolar power supplies. The dipole magnet is shown in Figure 6.4 showing both main and trim coils while Table 6.2 specifies the main magnet parameters.

Parameter	Nominal	Minimum	Maximum	Unit
Physical pole length (14")	0.356	-	-	m
Vertical pole gap	8	-	-	mm
Effective magnetic length	0.364	-	-	m
Pole width	40	-	-	mm
Number of dipoles per chicane	4	-	-	-
Length-integrated dipole field range	0.180 – 0.300	0	0.330	T-m
Vertical field (avg. over eff. magnet length)	0.494 – 0.824	0	0.907	T
Number of main-coil turns/magnet	378	-	-	-
Number of trim-coil turns/magnet	10	-	-	-
Trim field integrated strength/dipole ($\pm 1\%$)	0	-0.0033	0.0033	T-m

Table 6.2: Dipole magnet specifications.

Parameter	Nominal	Unit
Resistance/meter of square-cs AWG #7 copper wire at 50°C	0.0014	Ω/m
Copper's resistivity dependence on temperature (20°C ref.)	0.00386	per deg C
Total length of wire as main coil (est.)	435	m
Maximum excitation current of main coil (bipolar)	13.9	A
Total resistance of main coil at 50°C	0.687	Ω
Maximum thermal power dissipated per dipole magnet	130	W
Maximum total thermal power dissipated (8 dipole magnets)	1040	W

Table 6.3: Dipole magnet thermal heating estimate at max. field (with weak trim coils off).

Parameter	Nominal	Unit
Allowable quadrupole component at $x = 10$ mm	0.5	%
Allowable sextupole component at $x = 10$ mm	2	%
Allowable field strength inequality (unit to unit)	0.1	%
Remnant field at zero current (unit to unit)	0.5	G
Longitudinal positioning tolerance (unit to unit)	2	mm
Horizontal position tolerance (unit to unit)	2	mm
Vertical position tolerance (unit to unit)	0.5	mm
Roll tolerance (unit to unit)	2	mrads

Table 6.4: Magnet alignment and field quality tolerances (at 10.35 GeV).

6.2.1.1 Magnet Heat Load in Undulator Tunnel

When powered, each air-cooled dipole magnet will warm up until equilibrium is established (~ 8 hrs). Too much thermal power dumped into the undulator hall (20°C nominal) may change the precise field of the undulator K values and possibly distort component alignment. For this reason we have estimated the thermal power dissipation from all 8 dipole magnets in the tunnel running at maximum field. The estimate includes the resistance of the main coils, the magnet operating temperature, the excitation current, and the number of main-coil turns. A solid, square cross-sectional copper wire (AWG #7) is used. The resistivity of copper is taken at 50°C, assuming the coils reach this level after about 8 hours (measured in Feb. 2020). For this estimate the weak trim coils are off. A summary of these thermal analysis results are listed in Table 6.3. The full power dissipation is quite high and may need other compensation (e.g., water cooling or a smaller gap).

6.2.1.2 Magnet Alignment and Field Quality Tolerances

The magnetic field quality and alignment tolerances depend on the nominal beam size (20 μm) in the center two dipoles, the maximum transverse dispersion (11 mm), and the worst case relative beam energy spread (0.3% rms, assuming no deliberate beam chirp). These parameters are not so demanding, and only require modest tolerances. These are summarized in Table 6.4.

6.2.1.3 Prescribed Horizontal Alignment Offsets

The trajectory of the electron beam curves through each dipole magnet, as indicated in Figure 6.5, requiring a set of prescribed horizontal magnet offsets (Δx) to be applied during final alignment. This keeps the beam nearer to horizontal center, with the offsets summarized in Table 6.5.

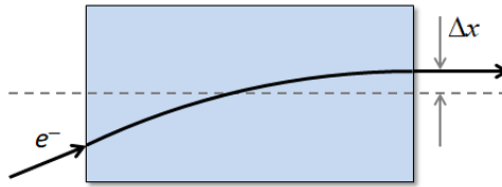


Figure 6.5: The electron beam trajectory curves through each magnet, requiring a set of prescribed horizontal magnet offsets (Δx) to keep the beam nearer to horizontal center through the full magnet.

Parameter	Nominal	Unit
B1 magnetic	1	mm
B2 magnetic	1	mm
B3 magnetic	1	mm
B4 magnetic	1	mm

Table 6.5: Dipole magnet horizontal alignment offsets with respect to the SASE axis.

6.2.1.4 Power Supply Performance Requirements

The main coil current is required to be bipolar for the purpose of de-gaussing the magnet before returning to SASE mode. The trim supplies are also bipolar to allow complete correction of the unit-to-unit current-to-field calibration errors. The requirements for the main (1) and trim (4) power supplies are summarized in Table 6.6. Note that the main-coil tolerances are based on a common field error (over all 4 dipoles) which displaces the beam only locally by $\pm 10 \mu\text{m}$ in the horizontal direction at chicane center.

6.3 Undulator System

The LCLS-II HXR undulator system consists of 34 girders, each of which rests on 5 cam movers. Each girder supports a quadrupole, an RFBPM, and a vacuum chamber (see Table 6.7). 32 girders also support a vertical polarizing undulator and 31 girders also support a permanent magnet phase shifter. The parameters of each undulator are listed in Table 6.8. The cam movers allow the upstream and downstream ends of each girder to be moved transversely to support beam-based-alignment, undulator system repointing, and a number of beam manipulation schemes. The used motion range is of up to about $\pm 1 \text{ mm}$ independently for either end of the girder; the precision is sub-micron. The girder in position 16 (HXR cell 28) carries the components of the hard x-ray self-seeding system (HXRSS), while the girder in position 9 (HXR cell 21) is empty, i.e. does not carry an undulator but only a quadrupole, an RFBPM, a vacuum chamber and vacuum equipment. This girder can be used to house the downstream X-ray optics and alignment system for the CBXFEL R&D project.

Parameter	Nominal	Unit
Trim coil set-ability, rms	0.05	% of trim-coil max. current
Trim coil stability, rms	0.05	% of trim-coil max. current
Main coil set-ability, rms	0.1	% of trim-coil max. current
Main coil stability, rms	0.1	% of trim-coil max. current

Table 6.6: Main (1) and trim (4) power supply requirements.

Table 6.7: LCLS-II Vacuum Chamber Parameters.

Parameter	Value	Unit
Type	Extruded Al	-
Inner Dimensions (heightxwidth)	$\pm 2.5 \times \pm 5.5$	mm
Surface Roughness Slope	< 0.20	mm
Water Cooling Channels	Included	-
Environmental Correction Coils	Included	-

Table 6.8: LCLS-II HXR Undulator Parameters per segment.

Parameter	Value	Unit
Type	NdFeB permanent magnet hybrid	-
Period Length	26	mm
Maximum K	2.44	-
Minimum Gap	7.2	mm
Number of Periods	130	-
Polarization Mode	Linear Vertical	-

The upstream X-ray optics and alignment system for the CBXFEL R&D project would need to be supported on the first HXR girder in position 1 (HXR cell 13) as shown in Figure 6.6, which is currently occupied with an LCLS-II HXR undulator. This girder will have to be relocated to the end of the HXR undulator line in the first of four still unoccupied cells at position 35 (HXR cell 47). This relocation will require the manufacture of two new pedestals and cam systems. A new girder, with vacuum chamber and support pedestals in addition to the components needed for the CBXFEL research project, would need to be manufactured to go into position 1 (HXR cell 13) as shown in Figure 6.7. It might be possible to take the required quadrupole and RFBPM that are needed for that girder from the spare pool. A phase shifter will not be required for that girder. The phase shifter that is currently on the first girder can be relocated to the end of HXR cell 46, since the last girder does not need a phase shifter. The new girder for the first position should be a copy of the HXRSS girder with the optical components replaced with components needed for the CBXFEL project. The girder that was moved from HXR cell 13 to HXR cell 47 had an extra RFBPM mounted to its upstream end. This RFBM needs to be relocated to the upstream end of the new girder that will be manufactured for HXR cell 13.

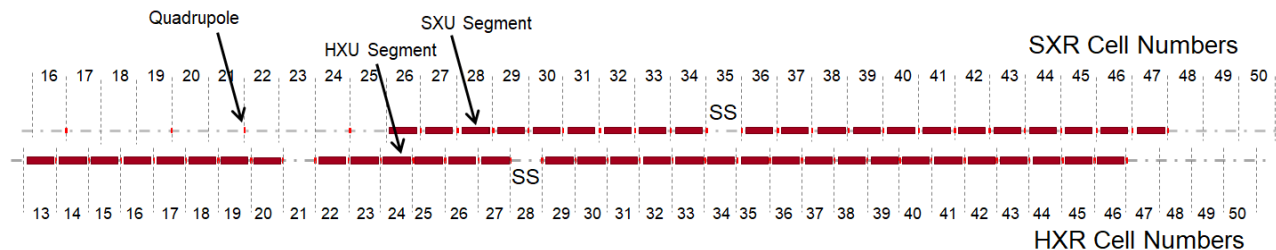


Figure 6.6: Present LCLS-II HXR undulator layout. Note: For clarity, this layout only shows undulator segments (large red rectangles and quadrupoles, small vertical red bars).

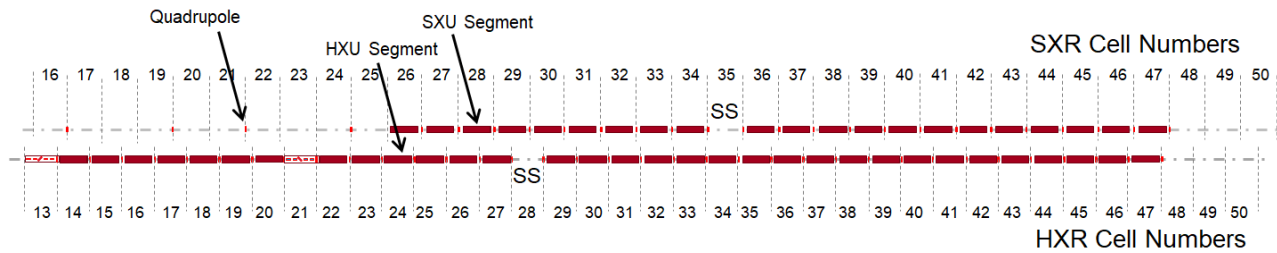


Figure 6.7: Proposed LCLS-II HXR undulator modifications to support the CBXFEL project. Graphics symbols indicating a girder, chicane dipoles and mirrors have been added to HXR cells 13 and 21 in this figure.

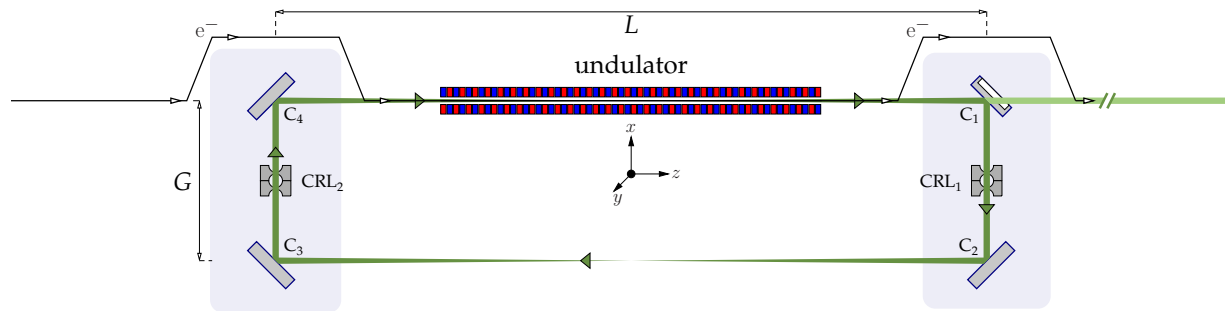


Figure 6.8: Layout of the CBXFEL x-ray cavity with the undulator.

6.4 X-ray Cavity System

6.4.1 Cavity system layout and components

Figure 6.8 shows the layout of a rectangular x-ray cavity together with the undulators planned for the CBXFEL project. The rectangular shape is chosen because of the constraints of the available space in the undulator hall. The photon energy cannot be tuned in such a cavity.

The x-ray cavity is composed of two back-scattering units comprising C_1 and C_2 crystals on the downstream side of the undulator and C_3 and C_4 crystals on the upstream side of the undulator, respectively. The crystals serve as Bragg-reflecting x-ray mirrors required to store, recirculate, and monochromatize x-rays in the cavity. Two x-ray focusing compound refractive lenses [1] CRL_1 and CRL_2 will be installed in the symmetry points of the back-scattering units to both control the transverse x-ray beam dynamics and stabilize the cavity.

The XFEL undulator composed of 7 undulator sections is placed between crystals C_4 and C_1 . The cavity has a length of $L \simeq 32$ m and a width of $G \simeq 0.65$ m. The round-trip path of x-rays in the cavity is $\ell = 2(L + G) \simeq 65.3$ m, and the round-trip time is $\tau = \ell/c \simeq 218$ ns, where c is the speed of light in vacuum.

The losses in the cavity must be kept minimal to ensure sufficient net gain, especially in the low-gain XFEL mode. For this purpose, all the crystals are required to be almost flawless diamond, with Bragg reflectivity close to 99% [2]. To ensure high reflectivity and stable strain-free mounting with good heat transport, the thickness of diamond crystals C_2 , C_3 , and C_4 is required to be >500 μm . Crystal C_1 is required to have the same thickness, but an indentation with a residual membrane of a < 25 μm thickness will be laser machined [3] on a small $\simeq 1$ mm^2 crystal area for outcoupling of $\gtrsim 1 - 10\%$ of the intracavity radiation through the membrane, as discussed in more details in Section 6.4.4.1.

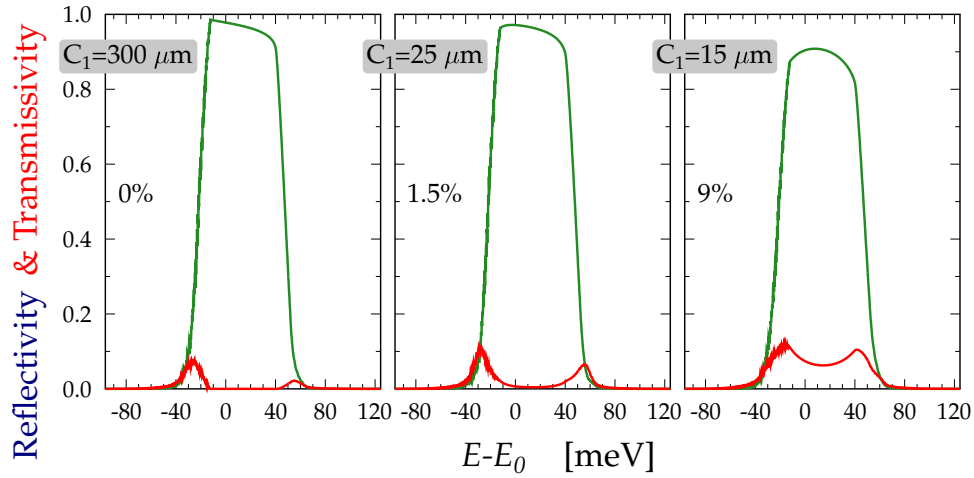


Figure 6.9: Spectral profiles of the perfectly aligned *empty* cavity after successive (400) Bragg reflection of x-rays from diamond crystals $C_2 \rightarrow C_3 \rightarrow C_4 \rightarrow C_1$ (green). Transmission profiles through crystal C_1 for various thicknesses of C_1 (red). Photon energy $E_0 = 9.831$ keV. Spectral bandwidth $\Delta E_{4 \times (400)} \simeq 69$ meV.

High crystal quality (i.e. absence of crystal defects) ensures high Bragg reflectivity. Crystal plates in the (100) orientation typically have the largest defect-free areas [4, 5, 6, 7]. We choose the lowest order allowed Bragg reflection (400) from crystal plates in this configuration. The rectangular geometry sets the Bragg angle of $\theta_{400} = 45^\circ$, which also determines the x-ray photon energy $E_{400} = 9.8319$ keV in the center of the Bragg reflection range, assuming the crystal temperature $T = 300$ K. The angular and spectral widths (FWHM) of a single (400) Bragg reflection range are $\Delta\theta = 8.8 \mu\text{rad}$, and $\Delta E = 91$ meV, respectively.

Green lines in Figs 6.9(a)-(c) show the spectral profiles of the perfectly aligned *empty* (*without gain*) cavity after the successive (400) Bragg reflection of x-rays from diamond crystals $C_2 \rightarrow C_3 \rightarrow C_4 \rightarrow C_1$. It is assumed here that an EM wave of unit spectral amplitude is incident on C_2 . The thickness of the crystal membrane of C_1 is assumed to vary from $25 \mu\text{m}$, to $15 \mu\text{m}$ in the calculations presented in Figs 6.9(a)-(c), respectively, with the purpose of varying the amount of the outcoupled power, as discussed in more detail in Section 6.4.4.1. In all scases the reflectivity remains high, but the cavity bandwidth shrinks to $\Delta E_{4 \times (400)} \simeq 69$ meV due to the four successive reflections.

Similar to the crystals, the focusing CRL elements are required to be low-loss, i.e., x-ray transparent. Beryllium paraboloidal biconcave lenses [8] are chosen as the focusing elements of the cavity and discussed in more detail in Section 6.4.3.3.

To keep cavity losses small x-rays should propagate in an evacuated space with residual pressure of 0.1 mbar or less.

6.4.2 Precision and Stability requirements

Producing an x-ray cavity with sufficient precision and stability to support FEL gain is one of the biggest challenges of the project. The essential requirement is that the various optical elements are positioned to sufficient accuracy over a cavity round-trip time such that the x-rays produced by the leading electron bunch are returned to be amplified by the trailing electron bunch. To reliably achieve this goal, the components must also maintain their accurate positioning over several seconds so that meaningful measurements and/or feedback controls can be applied.

Figure 6.10c shows the equivalent unfolded optical lattice of the x-ray cavity shown in Figure 6.10b and Figure 6.10a, which includes two focusing elements provided by compound refractive lenses (CRLs). This symmetric system has a matched cavity mode waist at two locations, w_1 and w_2 as noted in the figure, and can be easily analyzed within the framework of Gaussian beam ABCD optics. The coupling between the electron beam and the x-rays is typically optimized in the low-gain XFEL scenario when the radiation waist is in the middle of the undulator, as it is here, and when $Z_R \approx \langle \beta \rangle$, where Z_R is the x-ray pulse Rayleigh length and $\langle \beta \rangle$ is the average beta function of the electron beam in the undulator. Table 5.1 shows the main undulator and cavity parameters for the proposed experimental setup. For this design and the electron beam energy of ~ 10.3 GeV we have $\langle \beta \rangle \approx 22$ m for a matched electron bunch in the strong focusing undulator FODO lattice, and a matched waist size $w_1 \approx 30 \mu\text{m}$. Commercially available beryllium CRLs with a focal length of 28.4 m (at a 9.831 keV photon energy) support a stable cavity mode with a waist size of $w_1 \approx 32 \mu\text{m}$, which is close to the matched solution.

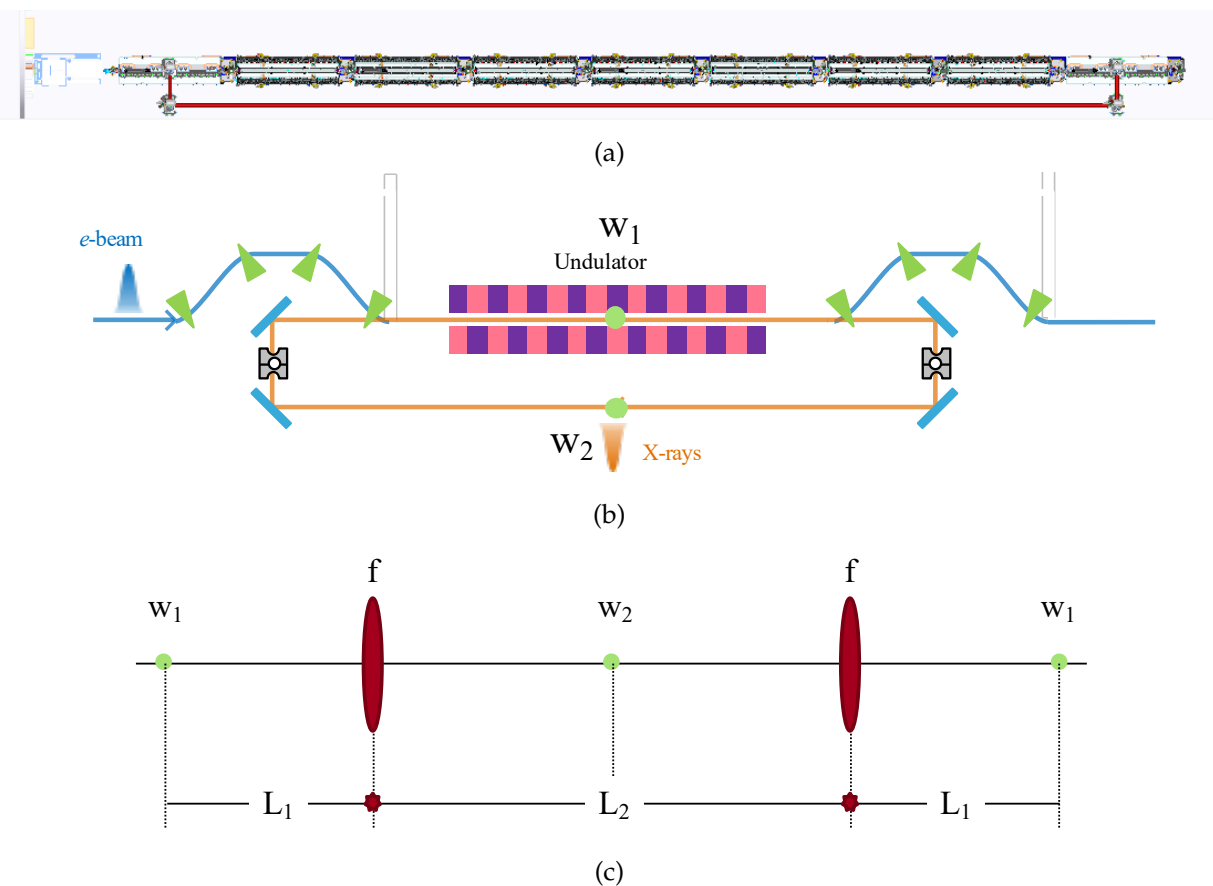


Figure 6.10: (a) Top view of the rectangular cavity. Note, HXRSS style chicanes are used in the model for illustrative purposes only. From left to right in the undulator beamline: TDUND, chicane and optics chamber, 7 HXR undulators, chicane and optics chamber. The solid red line illustrates the X-ray cavity return line. Not shown are two CRLs on the short ends of the rectangle (see (b) below). (b) Cartoon of the CBXFEL concept showing the paths of the electrons and photons. (c) Equivalent unfolded optical lattice of the X-ray cavity in (b) above.

The configuration of Fig. 6.10 is also suitable for the XRAFEL scenario. The waist size w_1 is very nearly the high-gain guided mode solution, and provides the best coupling between the electrons and photons. Another advantage of choosing w_1 to be close to the guided mode solution is that the

returned radiation at the entrance of the undulator after propagating through the cavity is larger than the gain-guided mode and is slightly converging. The larger field size at the entrance makes the XRAFEL slightly less susceptible to lateral and angular displacements (i.e. errors) of the seed radiation with respect to the second electron bunch trajectory.

The most stringent bound for the crystal angle tolerances can be determined using standard matrix optics. If the four crystals are displaced by the successive angles θ_{m1} , θ_{m2} , θ_{m3} , and θ_{m4} , the final error in position and angle of the radiation is given by

$$\Delta x = c_1\theta_{m1} + c_2\theta_{m2} + c_3\theta_{m3} + c_4\theta_{m4}, \quad (6.1)$$

$$\Delta x' = f_1\theta_{m1} + f_2\theta_{m2} + f_3\theta_{m3} + f_4\theta_{m4}, \quad (6.2)$$

where the c_i and f_i are functions of the optical cavity parameters (drift lengths, focal lengths, etc.) that are computed using the usual matrix analysis. For our cavity with two CRL lenses placed 33 m apart and with the readily available focal length of 28.4 m, we find that crystal angular errors displace the optical axis position by approximately $\Delta x \approx 22(\theta_1 + \theta_2) + 33(\theta_3 + \theta_4)$ meters, and in angle by about $2(\theta_3 + \theta_4) - 2.6(\theta_1 + \theta_2)$ radians. We can estimate the required mirror angle tolerances by assuming that the errors in mirror angles are independent and random, and performing a statistical tolerancing analysis using the Root Sum Square (RSS) method. In this case the error can be propagated in the usual way, and the RMS deviations for independent and equal magnitude angular errors of σ_m are given by

$$\sigma_x = \sqrt{(c_1^2 + c_2^2 + c_3^2 + c_4^2)\sigma_m^2} \approx 56\sigma_m \text{ m}, \quad (6.3)$$

$$\sigma_{x'} = \sqrt{(f_1^2 + f_2^2 + f_3^2 + f_4^2)\sigma_m^2} \approx 4.6\sigma_m. \quad (6.4)$$

The tolerance is then estimated by requiring the RMS deviation of the radiation in position and angle to be less than some fraction of the electron beam size (~ 20 microns) and divergence (~ 1.5 microrad). For example, if we require that the rms optical axis deviation to be less than one-eighth of the beam size and angle, then we find a crystal alignment error tolerance of $\sigma_m \lesssim 50$ nrad.

6.4.2.1 XRAFEL tolerances

The use of this statistical tolerancing method is somewhat questionable given the small number of independent sources of error (there are only four mirrors). Therefore, the high gain two-pass system has been evaluated with time-dependent and three-dimensional FEL simulations using GENESIS and Fourier optics propagation of the resulting fields through the optical cavity. Roughly 50 independent 2-pass simulations were performed where the angular errors of the four cavity mirrors were assumed to be independent and normally distributed with RMS fluctuations of $\sigma_m = 0, 100, 200, 300, 400$ nrad (also, see section 6.6.2.1 for additional performance detail). The $\sigma_m = 0$ nrad dataset indicates an aligned cavity and acts as the basis of comparison for the performance of the system under the various error scenarios studied here. The average gain of the second pass seeded interaction at the target photon energy over the first pass is as follows for each of the error cases listed above, respectively: 86, 88, 63, 62, 52. The apparent increase in the average gain from zero error to 100 nrad error is due to the limited number of simulations performed.

The reflectivity bandwidth of the diamond mirrors at the target photon energy produces a transform limited pulse length of ~ 25 fs (FWHM), which is comparable to the high peak current, high-gain electron beam pulse length (~ 50 fs, FW). Therefore, the temporal jitter between the electron beams between the first and second pass will impact the average second pass gain. In the high-gain scenario, the second pass electron beam will be seeded by a single longitudinal mode that roughly

covers the electron beam longitudinal profile. To first order then, a longitudinal mismatch between the returned radiation and the second pass electron beam will translate linearly to a degradation in the cavity bandwidth gain. This implies that if the RMS temporal jitter between the two electron beams is $\sigma_t = 25$ fs, roughly 68% of the shots will see at worst 50% of the nominal gain on average. This translates to an average second pass cavity bandwidth gain of 30 for a perfectly aligned cavity.

Therefore, based on the RSS tolerancing analysis, detailed 2-pass simulations, and temporal jitter considerations at the $\sigma_t = 25$ fs level, the RMS fluctuations in mirror angles must be less than 200 nrad. The average two pass gain in this case would be ~ 21 , which is roughly 25% of the perfectly aligned value in the absence of temporal two bunch electron beam time of arrival jitter.

6.4.2.2 XFEL tolerances

When the gain is low the tolerances should be reasonably well-estimated by combining the positional and angular error analysis of Eqs. (6.1)-(6.2). To improve the estimates further, we combine this analysis with the simulation results in Fig. 6.3(a) that showed how the gain depends upon relative displacement between the radiation and electron bunch. Figure 6.3(a) indicates that the excess photons within the crystal bandwidth are reduced by less than 10% provided the displacement $\Delta x \lesssim 8$ micron. If we then require this limit to be at the three-sigma level,

$$8 \mu\text{m} = 3\sigma_x = 3\sqrt{c_1^2 + c_3^2 + c_3^2 + c_4^2\sigma_m^2}, \quad (6.5)$$

then we infer that $\sigma_m \approx 50$ nrad.

To insure that a 50 nrad angular stability requirement is sufficient for the the XFEL, we have tested this case with three-dimensional FEL simulations using GENESIS. For these simulations we ran 60 independent instances of crystal misalignments assuming that they have random errors with $\sigma_m \approx 50$ nrad. The results are summarized with a histogram of the output photon number in the narrow crystal bandwidth in Fig. 6.11. We have found that observed signal and its variations are nearly the same as that of the ideal cavity, meaning that the random fluctuations are dominated by the spontaneous radiation within the narrow bandwidth and not the crystal errors.

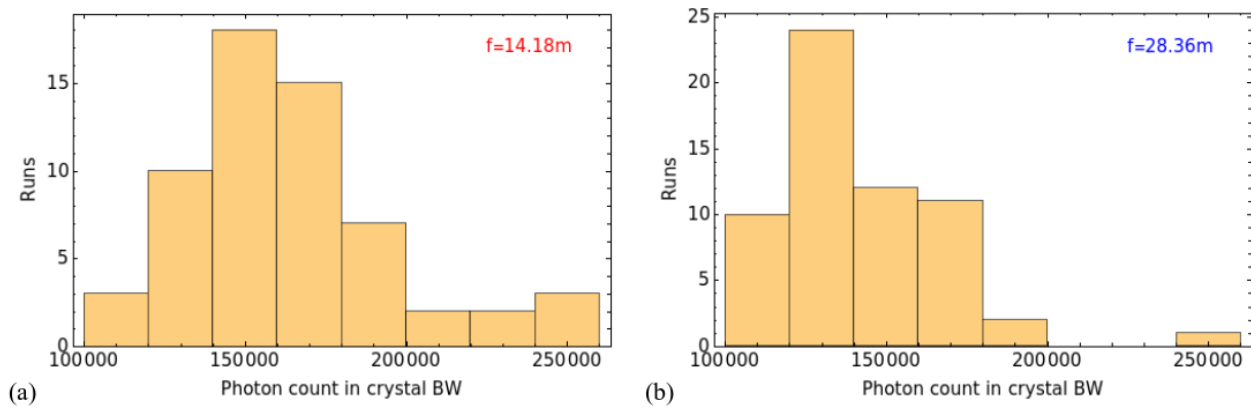


Figure 6.11: Histogram of expected photon output from the second pass assuming that the crystal errors are randomly distributed with a rms error of $\sigma_m = 50$ nrad for a CRL focal length of (a) $f = 14.18$ m and $f = 28.36$ m. The observed variation is consistent with random fluctuations of the spontaneous undulator radiation within the crystal output.

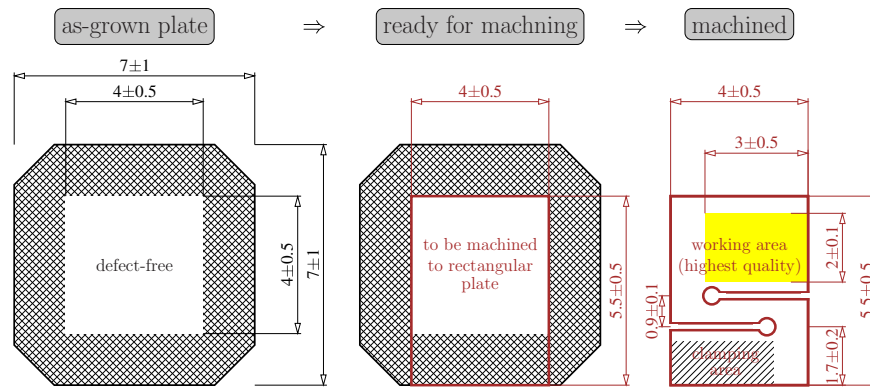


Figure 6.12: Drawings of the required diamond crystal plates: as grown, marked up for machining, machined.

6.4.3 X-ray optics elements

6.4.3.1 Diamond crystal optics: specification, characterization, and machining

The requirement of low losses in the x-ray cavity demands diamond crystals featuring a very high $\simeq 98\%$ x-ray reflectivity and small wavefront distortions of not more than $0.2 \mu\text{rad}$ (rms). The last number is 1/10th of the rms angular divergence of the XFEL beam. This number is also in agreement with the tolerances on the angular stability of cavity crystals, see Section 6.4.2.2. Wavefront distortions may result from crystal strain due to different origins (e.g., crystal defects, machining, and mounting), which in turn result in Bragg plane slope errors and reduced reflectivity. Bragg reflectivity is difficult to measure directly, but can be inferred from measurements of the Bragg plane slope errors that can be performed using the APS sequential x-ray Bragg diffraction topography setup [9], also known as rocking curve imaging (RCI).

To meet the high reflectivity, low wavefront distortion requirements, defects within the diamond crystals such as inclusions, dislocations, stacking faults, etc, shall be minimized. Ideally, within a central area of the (100) growth sector the crystal should be free of any of the aforementioned defects. This is because even though the footprint of the anticipated x-ray beam is much smaller, crystal strain originates from defects can propagate a few millimeters. Therefore, a stringent requirement on the size of the defect-free area is much desired. The desired overall size of the crystal plate of $\simeq 7 \times 7 \text{ mm}^2$ would then allow space for introducing the strain relief features as well as area for stable clamping, as indicated in Fig. 6.12. Other requirements are summarized in Table 6.9.

More specific details on the crystal optics procurement, characterization, and machining are listed below:

1. The samples delivered by the manufacturer (Sumitomo Electric Industries) will be first screened by SPring-8 with x-ray white-beam topography (or equivalent) for crystal defects (dislocations, stacking faults, inclusions, etc.) to down select the highest quality crystals for further use in the CBXFEL project.
2. Samples having the largest defect-free areas will be selected for further characterization.
3. RCI, and potentially high resolution wavefront sensing, will be used to characterize selected samples for lattice deformations. Crystals with lowest Bragg plane slope errors in the working area will be selected for further processing.

	Requirement	Value
1.	All plates are cut from the top part of the diamond stone furthest from the seed	
2.	Orientation	(100), miscut angle $< 0.1^\circ$
3.	Crystal plate size	$\simeq 7 \times 7 \text{ mm}^2$
4.	Plate thickness	$550 \pm 50 \mu\text{m}$
5.	Defect-free area of the (100) growth sector	$\simeq 4(\pm 0.5) \times (\pm 0.5) \text{ mm}^2$
6.	Bragg plane slope error	$< 0.2 \mu\text{rad}/\text{mm}^2$ in the working area $\simeq 3 \times 2 \text{ mm}^2$
7.	Surface roughness to	5 nm
8.	Number of plates	$\simeq 8$

Table 6.9: Diamond crystal specifications

4. The selected diamond crystal candidates (Qty. 6-8) will be cut using the laser micromachining techniques to $4 \times 6 \text{ mm}^2$ (H×V) rectangles with the upper $4 \times 3 \text{ mm}^2$ area being highest crystal quality.
5. The in-plane orientation of the crystals will be determined such that the rectangles are oriented in a direction to avoid excitation of multiple-beam diffraction which is detrimental for the cavity performance.
6. ‘Drumhead structures’ (explained in later sections on cavity out-coupling mechanisms) with $18 - 20 \mu\text{m}$ thin membranes will be machined using laser ablation and finished by dry plasma etching.
7. In addition, mounting through holes and strain relief cuts will be machined in all selected samples. The machining and etching will be performed by external vendors in the USA.
8. The machined samples will be annealed at high temperatures using the furnaces available at the APS in order to remove strain and crystal deformations introduced by the machining.
9. The samples will be mounted on Argonne-designed diamond CVD crystal holders that will be machined by external vendors.
10. The mounted samples will undergo final screening for residual crystal deformations in the working upper area using the x-ray RCI setup and the x-ray wavefront sensor setup.
11. The samples with lowest crystal slope errors ($< 0.2 \mu\text{rad}/\text{mm}^2$ within the working area) will be selected for use as cavity crystal mirrors.

6.4.3.2 Crystal temperature stability

A temperature change δT of a crystal results in a variation of the interplanar distance d_H , corresponding to atomic planes with reciprocal vector H , by $\delta d_H = d_H \beta \delta T$, where β is the crystal linear temperature expansion coefficient ($\beta = 10^{-6} \text{ K}^{-1}$ for diamond at room temperature) and therefore

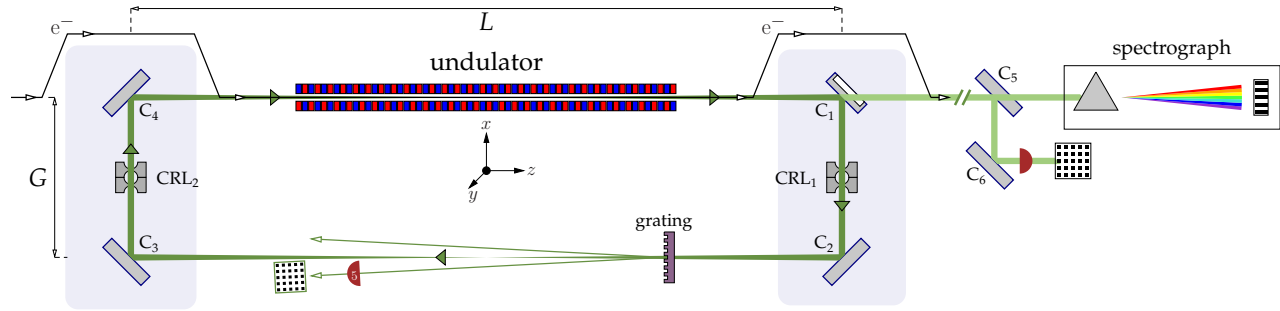


Figure 6.13: Layout of the CBXFEL x-ray cavity showing two options for output couplers: the thin permeable diamond crystal C_1 , and the diamond diffraction grating.

in a shift of the center of the angular Bragg reflection curve by $\delta\theta = (\delta d_H/d_H) \tan\theta = \beta \delta T \tan\theta$. To stay on the top of the Bragg reflection curve having an angular width of $\Delta\theta = \epsilon_H \tan\theta$ (here $\epsilon_H = \Delta E_H/E$ is a Bragg reflection invariant the relative spectral width of the Bragg reflection in symmetric scattering geometry) we require that $\delta\theta \lesssim \Delta\theta/10$, or

$$\delta T \lesssim \frac{\epsilon_H}{10\beta}. \quad (6.6)$$

In a particular case of the diamond (400) Bragg reflection with $\epsilon_{400} = 8.7 \times 10^{-6}$, we obtain that the temperature of all cavity crystal have to be maintained the same to an accuracy of $\delta T \lesssim 0.8$ K.

6.4.3.3 Focusing optics

Cavity stability discussed in Secs. 6.4.2 requires that the focusing elements placed between the crystals in the backscattering units (shown in the figure above) have a focal length in the range of $f \simeq 30 \pm 15$ m. Generally speaking, the beam loss by each focusing element shall be less than 1%, and the wavefront distortion produced by the lenses shall be below $\lambda/20$.

The x-ray beam size at the focusing elements is about $100 \mu\text{m}$ in full width. The large focal length and the small transverse beam size make beryllium compound refractive lenses (CRL) [8] ideally suitable[10], ensuring high x-ray transparency and low aberration. The beryllium lenses are commercially available in several standard radii of curvature. Table 6.10 lists several available R values and corresponding focal length at the cavity nominal photon energy of $E = 9.831$ keV. Large-radius lenses can be used to fine-tune the effective radius-of-curvature of the stack when combined with small-radius lenses to achieve accurate control of the focal lengths.

6.4.3.4 Intracavity beam sampling optics

In the cavity system layout as shown in Fig. 6.13, a minimally-invasive beam sampler is conceived to provide in-situ diagnostic capabilities for the x-ray cavity. This beam sampling functionality can be achieved with a transmission diamond grating fabricated on a thin diamond substrate. The primary requirements for the grating performance are listed below.

1. greater than 0.5% transmission into each of the ± 1 diffraction orders for use in diagnostics. This would provide sufficient intensity to perform the ring-down measurement using a fast point detector, i.e. an avalanche photo diode, and for beam position/profile characterization and monitoring.

	Radius of curvature R [μm]	Focal length f [m]
1.	50	7.089
2.	100	14.177
3.	200	28.355
4.	300	42.523
5.	500	70.720

Table 6.10: Radius of curvature R of the standard commercially available from RXOPTICS GmbH beryllium paraboloidal biconcave lenses and their focal length f for photons with 9.831 keV energy.

2. total beam absorption loss below 5%, ideally below 2%. This is to minimize the cavity loss and deliver the highest-intensity seed beam back into the undulators.
3. wavefront distortion induced by the grating in both the transmitted and sampled x-ray beams shall be lower than $\lambda/20$.

We also note that in the cases when cavity loss needs to be minimized as much as possible, one should be able to retract the beam sampler out of the beam path.

6.4.4 Cavity out-coupling mechanisms

Two outcoupling methods are presented here, schematically shown in Fig. 6.13. In the first case, the intracavity x-ray power is coupled out through a thin permeable diamond crystal C_1 as discussed in Section 6.4.4.1. In the second case discussed in Section 6.4.4.2, a diamond diffraction grating is used. Other out-coupling mechanisms are also being explored, including an electron beam based method that employs a (quasi-)achromat to rotate the electron microbunching wavefronts in order to redirect the coherent X-ray radiation to an angle outside of the diamond crystal's rocking curve, or, in XRFEL mode, by replacing the thin membrane in the diamond crystal with a center hole that might outcouple significant radiation power. Nevertheless, we regard the drumhead-diamond scheme (Section 6.4.4.1) as the baseline design for the CBXFEL project. We consider other schemes including the transmission grating to be R&D topics at the initial stage of the project.

6.4.4.1 Thin diamond crystal

A partially-reflective cavity mirror is a standard method of outcoupling in laser physics. It can be extended to a hard x-ray regime as well. Indeed, a similar approach was proposed for coupling photons out of the XFEL optical cavities by using thin, permeable crystal mirrors [11, 12, 13]. One of the Bragg-reflecting crystal mirrors is thin, just a few extinction lengths $\bar{\Lambda}_H^{-1}$, and is used as a permeable mirror with reduced reflectivity. This method is very often limited to extracting less than 10% of the cavity power due to practical constraints on the minimal crystal thickness. Hence, while the drumhead outcoupling will serve either the XFEL or XRFEL mode of the two-bunch CBXFEL project, it is ultimately more suited to the low levels of outcoupling required by a low-gain XFEL.

Figure 6.9 shows spectral reflection profiles (green lines) of the *empty* cavity (no undulator) and spectral profiles of transmission (red line) through diamond crystal C_1 of different thicknesses d . The

¹Extinction length is a characteristic depth of penetration of x-rays in Bragg diffraction in crystals. Here we are using the extinction length as defined in [14]. In other texts, e.g. in [15] an alternative definition is used $\Lambda_H = 2\pi \bar{\Lambda}_H$.

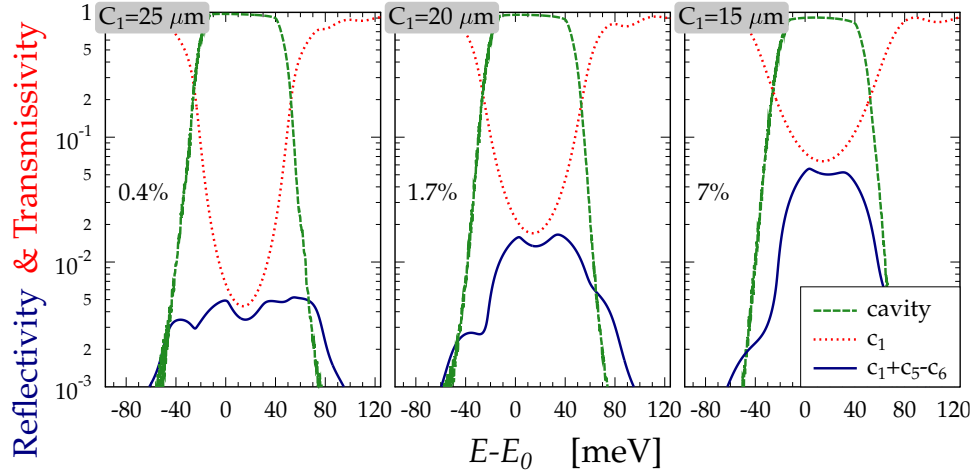


Figure 6.14: Spectral profiles of the perfectly aligned cavity after successive (400) Bragg reflection of x-rays from diamond crystals $C_1 \rightarrow C_2 \rightarrow C_3 \rightarrow C_4$ (green), similar to those in Fig. 6.9; however, shown here on the logarithmic scale. Transmission profiles through crystal C_1 for various thicknesses of C_1 (red) and through a C_5 - C_6 monochromator (navy) with $C_5=C_6=\text{Si}(531)$. Photon energy $E_0 = 9.831$ keV. Spectral bandwidth $\Delta E_{4 \times (400)} \simeq 69$ meV.

thinner the crystal, the smaller is the reflectivity, and the larger is the transmitted, outcoupled power. The transmissivity at the central photon energy $E = E_0$ changes exponentially as

$$T(0) \simeq 4 \exp(-d/\bar{\Lambda}_H), \quad (6.7)$$

in the “thick” crystal limit $d > \bar{\Lambda}_H$ [16]. For example, a 5%-transmissivity is achieved if $d \simeq 4.4\bar{\Lambda}_H$. For the 400 Bragg reflection in diamond with $\bar{\Lambda}_{400} = 3.6 \mu\text{m}$ [14], the required crystal thickness $d = 16 \mu\text{m}$ is quite small

The presented picture in Fig. 6.9 is not completely correct, because in our case the cavity is not empty. The undulator installed between crystals C_4 and C_1 is a broad-band x-ray source at the outset of the lasing process. Therefore, the spectrum profile of transmission through C_1 is better represented by the red dotted curves in Fig 6.14. The increased transmission at $E = E_0$ will be observed on the large background of x-rays with photon energies outside the cavity reflection profile (green lines).

There are two ways to deal with this “background” problem. In the first case a single shot spectrograph can be used to observe shot-to-shot evolution of the x-ray spectrum within the cavity reflection profile, as discussed in Section 6.9. The second possibility is to install into the transmitted beam an x-ray monochromator with a bandwidth slightly smaller than the cavity reflection profile, which would filter out the photons in the cavity bandwidth, and allow measuring pulse by pulse the time dependence of outcoupled power.

Dark blue lines in Fig. 6.14 present the spectra of x-rays filtered through a two-crystal non-dispersive monochromator composed of Si crystals in the 135 Bragg reflection. The spectra are calculated for different thicknesses of diamond crystal C_1 . The photons transmitted through the monochromator crystals are background-free. Therefore, a detector with a ns-time resolution installed downstream (BIM₄) will be able to detect the time evolution of the outcoupled power.

Manufacturing and handling such thin diamond crystals is challenging. One way to overcome these hurdles without degrading Bragg diffraction performance is to use the drumhead crystal design [3] as shown in Fig. 6.15. Drumhead crystals are monolithic crystal structures composed of a thin crystal membrane in the middle that is surrounded and stabilized by a solid thick collar of crystalline

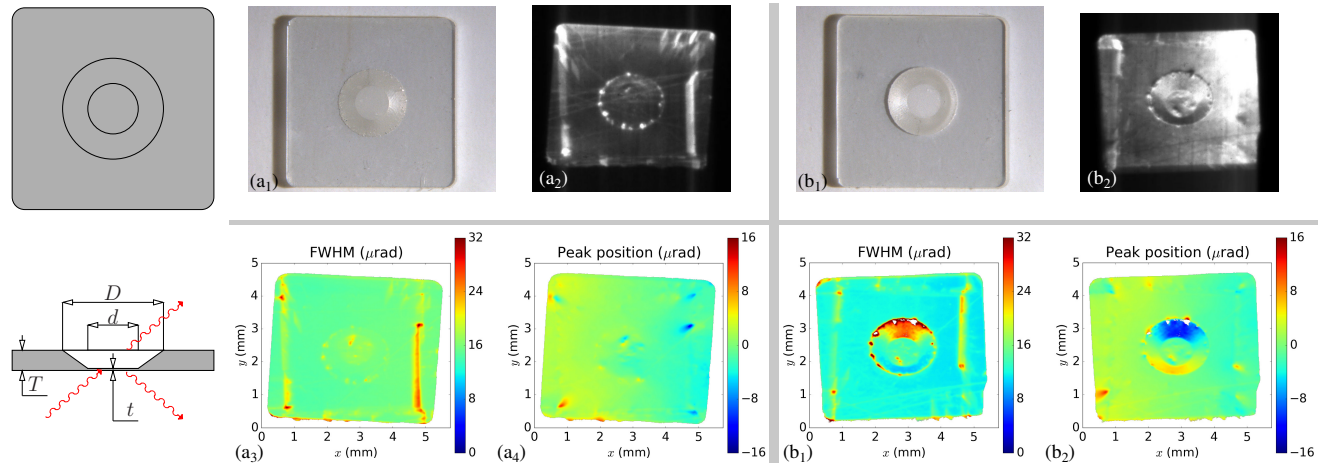


Figure 6.15: Schematic drawing of a drumhead crystal and Bragg diffraction geometry (left). Photographs, Bragg reflection images and rocking curve maps of a diamond drumhead crystal with a $26 \pm 2 \mu\text{m}$ thick, 1-mm in diameter membrane, and with a $340 \mu\text{m}$ -thick surrounding collar after high-temperature annealing.

material. This design enables mechanically stable and strain-free mounting of a thin membrane that also maintains efficient thermal transport. Almost flawless diamond drumhead crystals with a $25 \mu\text{m}$ thin membrane in the (100) orientation were manufactured by picosecond laser milling and characterized, as shown in Fig. 6.15. Thinner membranes can be fabricated by adding a final step of plasma dry etching.

6.4.4.2 Diamond transmission grating

A thin diamond crystal controls the out-coupled fraction by adjusting the crystal thickness. In contrast, a transmission grating creates new branches of x-ray beams at different angles from the original beam, and by choosing this angle to be larger than the reflection angular acceptance of the cavity crystal, e.g., C_1 , the branched x-rays will be transmitted downstream. The out-coupling efficiency can be adjusted by varying the grating structure height, which in turn varies the induced phase shift. Like the beam sampler, the 1st order diffraction efficiency can be adjusted between below 1% up to more than 30%. This offers flexibility, as the grating can be tailored to the needs of both the high-gain and low-gain systems, as illustrated in Figure. 6.16.

The technology for fabricating such gratings with low loss and minimal wavefront distortion using CVD diamond has matured as has been reported by Katayama *et al.*, Makita *et al.*, and Li *et al.* [17, 18, 19]. The performance requirement will be similar to that of the grating beam sampler mentioned earlier with low absorption loss ($< 5\%$) and high degree of wavefront preservation ($< \lambda/10$), except that the efficiency of the 1st order diffraction will likely need to be higher, in the range of a few percent for XFEL and may be tens of percent for XRAFEL.

6.4.5 X-ray Diagnostics

X-ray diagnostics are essential for establishing and monitoring the alignment of the cavity to within the tolerances defined above. A potential set of diagnostic tools is shown in the CBXFEL cavity layout in Figure 6.17. These diagnostics measure beam intensity, position, profile, as well as spectral content at various locations of the CBXFEL system. All the diagnostic tools shall satisfy the system



Figure 6.16: Two potential optical layouts for cavity out-coupling using low first-order-efficiency transmission grating. (a) Out-coupling the ± 1 diffraction orders while keeping the 0th order inside the cavity. (b) Out-coupling the 0th order while keeping one of the 1st order diffraction as the circulating beam path. This will lead to a cavity layout that deviates slightly from a perfect rectangle (angles in Figure highly exaggerated). For a low-diffraction-efficiency grating configuration (b) is more suited to a high gain FEL.

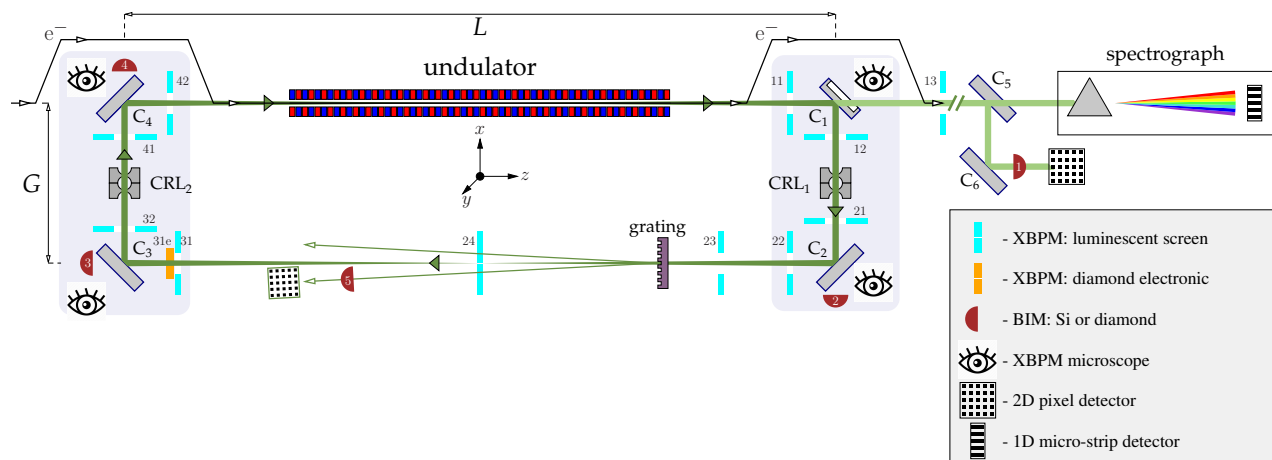


Figure 6.17: CBXFEL x-ray cavity with diagnostic tools.

vacuum requirements. In addition, the performance of the diagnostic tools should not be detrimentally affected by the radiation and electromagnetic background in the vicinity of the electron beam.

6.4.5.1 X-ray intensity diagnostics

X-ray intensity diagnostics are needed for two primary purposes:

1. To locate the correct crystal angles that meet the Bragg condition for the chosen wavelength.
2. To perform the cavity ring-down measurement.

In order for the intensity diagnostics to be set correctly for Bragg conditions, the detectors must function with a photon flux as high as the whole pulse (estimated to be as high as 10^7 photons per

pulse, or 10^9 per second), and as low as 10^3 per pulse or 10^5 per second. We therefore require those detectors to have a linear response range up to 10^7 photons per pulse and a sensitivity down to 100 photons. All detectors shall be read out in pulse-resolved mode.

For the ring-down measurement, as it will likely be performed with either a partially absorbing thin detector in the beam, or performed in the diagnostic branch picked up by the grating beam sampler, we envision the need for two orders of magnitude higher sensitivity compared to the Bragg-alignment detectors in order to compensate for the lower photon flux. This can potentially be relaxed if the ring-down was only to be performed with a single bunch high-peak-current beam mode with higher x-ray flux. This would then translate to the same sensitivity and dynamic range requirement as mentioned in the previous paragraph. In addition, time resolution much better than the cavity round trip time of ≈ 220 ns. We will set the requirement to be better than 10% of the cavity round trip time to be 20 ns.

6.4.5.2 X-ray position and profile diagnostics

XBPM #	Field of view [mm]	Resolution [μm]	Sensitivity [ph/s]	motion range (precision) [mm (μm)]	Sensor	Remark
11	5×5	10	$10^9 - 10^{10}$	12×12 (1)	D:B or YAG:Ce +Ø250 μm hole	initial alignment
42, 13	5×5	10	$10^5 - 10^8$	12×12 (1)	YAG:Ce/GOS:Pr +Ø250 μm hole	initial alignment
12,21,22, 23, 31, 32, 41	10×10	10	$10^5 - 10^8$	12×12 (1)	YAG:Ce/GOS:Pr or Si:quadrant +Ø250 μm hole	initial alignment
31e	3×3	0.1	$10^5 - 10^8$	12×12 (1)	CVD (Sydor) 30 μm	final algnmt + ns- & nrad- -sensitivity
24	10×10	<5	$10^5 - 10^8$	12×12 (1)	D:B 20 μm	final algnmt + beam imaging

Table 6.11: List of x-ray beam position monitors (XBPMs) and their specifications. The following abbreviations are used: D:B=boron doped diamond; YAG:Ce= $\text{Y}_5\text{Al}_5\text{O}_{12}:\text{Ce}$; GOS:Pr= $\text{Gd}_2\text{O}_2\text{S}:\text{Pr}$. For the cavity alignment, an averaged (1 Hz or 10 Hz) signal from the diagnostics is sufficient. The dynamic range of these diagnostics will be flux limited, extended dynamic range can be achieved with long averaging times.

X-ray intensity and position diagnostics are required to align the cavity. They can also provide beam profile information which can be used to further access the quality of cavity optics. As shown in Figure 6.17, diagnostics should ideally be positioned upstream and downstream of each optical component. These diagnostics shall be minimally invasive in terms of absorption losses or wave-front distortion while maintaining its sensitivity and spatial resolution. We thus envision a majority of the diagnostics utilizing central apertures (≈ 250 μm) to allow the beam to pass through undisturbed when the cavity is aligned. When the cavity is misaligned, the beam will impinge on the off-center active area and generate a readout signal to indicate which direction the beam is misaligned off-center. Alternatively, a thin scintillator screen without a central aperture, but with sufficiently

low absorption, can potentially be used (e.g., 24 in Figure 6.17) to enable final precision alignment. A candidate set of diagnostic requirements and potential measurement systems is presented in Table 6.11. The candidate X-ray beam position monitors (XBPMs) can be of electronic or luminescent in nature. Each type of XPBM has advantages and disadvantages and will be deployed based on specific requirements at each location.

- *Electronic silicon or diamond X-ray quadrant beam position monitors (XBPMs)*: They measure beam intensity and position. These have the highest sensitivity but relatively lower spatial resolution (especially with a central hole) compared to an imaging system.
- *Luminescence based x-ray profile monitors*: These use X-ray scintillator screens coupled with microscope optics and 2D imaging sensors. They provide not only beam intensity, position, but also beam profile information. These systems have good spatial resolution, but lower sensitivity than electronic XBPMs.
- *The diamond crystals of the cavity itself*: The luminescence of the cavity diamond crystals can also be used for alignment purpose by imaging with an optical microscope.

Generally, at key alignment locations 1 μm positional sensitivity and 10 μm spatial resolution are needed to be sensitive to the final crystal angular adjustment at the 100 nrad level. It is desirable to achieve these imaging performances with a maximum of 1-2 second exposure time.

6.4.5.3 Spectral diagnostics

Understanding of the FEL amplification process within the x-ray bandwidth supported by the cavity requires spectral diagnostics that has higher energy resolution than the cavity bandwidth of ~ 70 meV. Pulse-resolved average spectra can be measured by scanning a high resolution monochromator, e.g., as formed by C_5 and C_6 shown in Figure 6.13. This monochromator can be also installed within the x-ray cavity and perform the measurement on one of the intracavity beam samples.

In addition, spectra of the radiation after each round trip can be monitored shot-to-shot and after each round trip using a meV-Resolution single-shot spectrograph. The spectrograph shall ideally satisfy the following requirements:

- A $\simeq 70$ -meV cavity bandwidth requires a spectrograph with a $\lesssim 10\text{--}20$ meV spectral resolution.
- Sensitivity sufficient for x-ray pulse intensity level of $\simeq 10^3$ ph/pulse (XFEL) and $\simeq 10^4 - 10^5$ ph/pulse (XRFEL).
- Ability to resolve the two subsequent pulses 220-ns apart.

There are two primary types of single-shot spectrographs. The schematic of spectrographs based on principles of spectral filtering [20, 21] is shown on the left graph of Fig. 6.18, while the right graph presents the schematic of spectrographs based on angular dispersion [22, 23, 24]. Table 6.12 presents main features of the both types of the spectrographs for comparison. Spectrographs using angular dispersion principle feature higher efficiency and higher resolution are more appropriate for CBXFEL applications. Figure 6.19 shows an example of the optical design of the angular dispersive spectrograph appropriate for the current CBXFEL project, featuring a 185-meV broad spectral window of imaging and 8-meV resolution, assuming that strip-detector GOTTHARD-II [25] with a 25- μm spatial resolution and a 4.5-MHz frame rate is used.

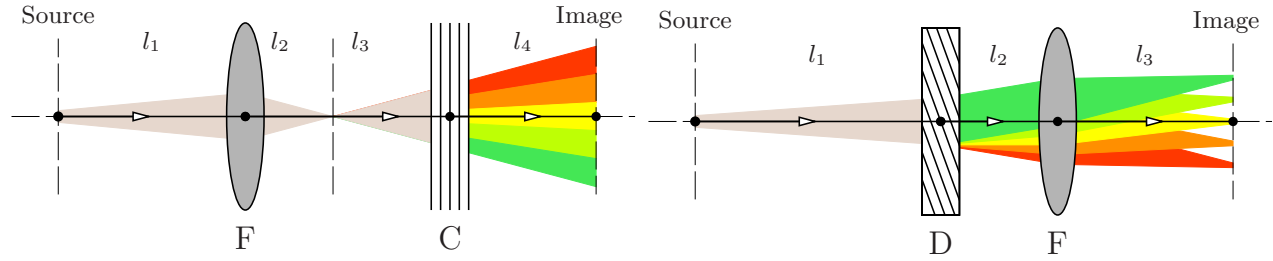


Figure 6.18: Schematics of spectrographs based on principles of spectral filtering [20, 21] (left) and angular dispersion [22, 23, 24] (right).

	Spectral filtering	Angular dispersion
1.	Narrow-band ($\Delta E \gtrsim 20$ meV) and small-acceptance-angle ($\Delta\theta \simeq 10$ μ rad) Bragg reflection.	Broad-band asymmetric Bragg reflections.
2.	Large incident beam divergence $\Omega \gtrsim 1$ mrad	Large angular dispersion rate.
3.	Large spectral window of imaging $E\Omega/\tan\theta \gtrsim 1$ eV.	Spectral window of imaging $W \lesssim 200$ meV
4.	Low efficiency $\simeq \Delta\theta/\Omega \simeq 10^{-2} - 10^{-3}$.	High efficiency $\simeq 50\%$
5.	Ultimate spectral resolution limited to $\Delta E \gtrsim 20$ meV.	Ultimate spectral resolution $\lesssim 1$ meV limited by source size and detector spatial resolution
6.	Unscalable to cope with ultimate XFEL requirements.	Scalable to cope with ultimate XFEL requirements.
	Low efficiency, medium resolution solution. Appropriate for SASE	High efficiency, high resolution solution Appropriate for CB-XFEL

Table 6.12: Basic features of the “spectral filtering” and of the “angular dispersive” type of spectrographs are compared.

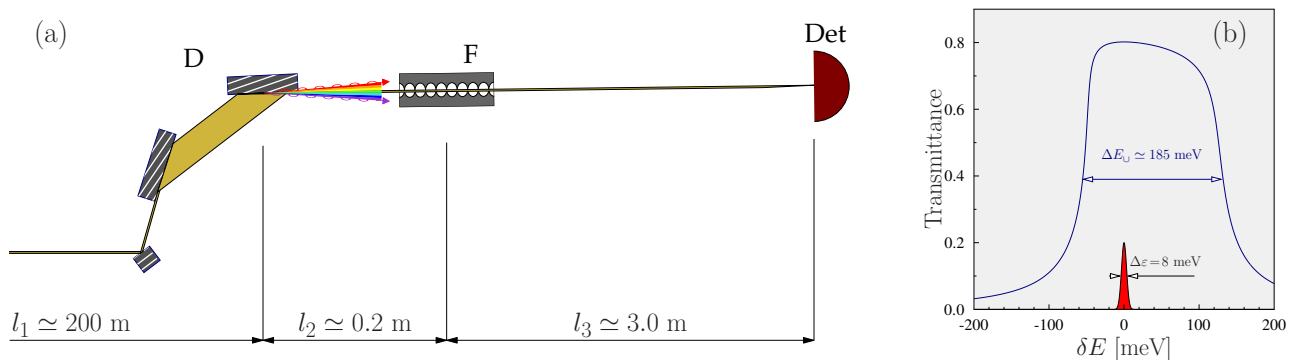


Figure 6.19: Optical scheme of an angular dispersive spectrograph for CBXFEL composed of a three-crystal dispersing element, focusing CRL and pixel detector (a) together with a graph (b) showing the spectrograph’s window of imaging of 185 meV and 8-meV spectral resolution.

• Spectral resolution [23] (ultimate)	$\Delta\varepsilon = \frac{\Delta x}{l_1} \frac{1}{\mathcal{D}}$	$\lesssim 1 \text{ meV}$
(detector-limited)	$\Delta\varepsilon_D = \frac{\Delta x_D}{l_3} \frac{1}{\mathcal{D}}$	$\simeq 8 \text{ meV}$
• Spectral window		$\simeq 185 \text{ meV}$
• Source size	Δx	$\simeq 100 \text{ }\mu\text{m}$
Detector pixel size	Δx_D	$\simeq 25 \text{ }\mu\text{m}$ [25]
Dispersion rate	\mathcal{D}	$\simeq 1 \text{ }\mu\text{rad/meV}$

Table 6.13: Design parameters of the angular dispersive spectrograph presented in Fig. 6.19.

6.4.6 Cavity Alignment Procedure

In brief, the alignment of the x-ray cavity can be conceptualized as a $3\text{D} \Rightarrow 2\text{D} \Rightarrow 1\text{D} \Rightarrow 0\text{D}$ procedure, with the following major steps:

- 3D:** Installing all crystal mirrors, CRLs, and XBPMs into nominal (x, y, z) positions with a $\simeq 20\text{--}30 \text{ }\mu\text{m}$ accuracy and guiding x-rays through all the components.
- 2D:** Reducing 3D to 2D x-ray beam trajectory. All the beams are forced into the nominal cavity plane by properly aligning roll/tilt of the cavity diamond crystals.
- 1D:** Reducing 2D to 1D beam trajectory. After the beam has made several round-trips, one can achieve convergence of the beam paths by fine tuning the crystal positions $[x, z]$ and pitch/Bragg angles
- 0D:** Adjusting the round-trip cavity length by translating a pair of crystals and the corresponding focusing optics and diagnostics on one side of the rectangle and monitor the XFEL gain.

The single e-bunch operation will be used for steps up to 1D, and the two-bunch operation will be used only in 0D.

The key alignment component accuracy and precision requirements are listed below.

- All luminescent XBPMs (except for XBPM_{24}) have holes to guide the correct x-ray beam trajectory, with each hole having a diameter of $7\sigma_x = 250 \text{ }\mu\text{m}$.
- At least two XBPMs are required in each branch, since they define both the position and direction of the x-rays in each branch.
- The (x, y, z) coordinates of the XBPM holes of all XBPMs and crystals in their “home” positions (determined by cap-sensors and the interferometer system) are measured with a μm -accuracy in the reference system of each station using a μm -precision coordinate measuring machine (CMM).
- XBPM_{11} and XBPM_{42} are the reference XBPMs in the downstream and upstream stations, respectively. They are installed onto the undulator axis by the translation and rotation of the stations as the whole.
- The stations are properly pre-aligned when XBPM_{11} and XBPM_{42} are on the undulator axis, while XBPM_{22} and XBPM_{31} are parallel to the undulator axis to $\simeq 2 \text{ }\mu\text{rad}$ accuracy.

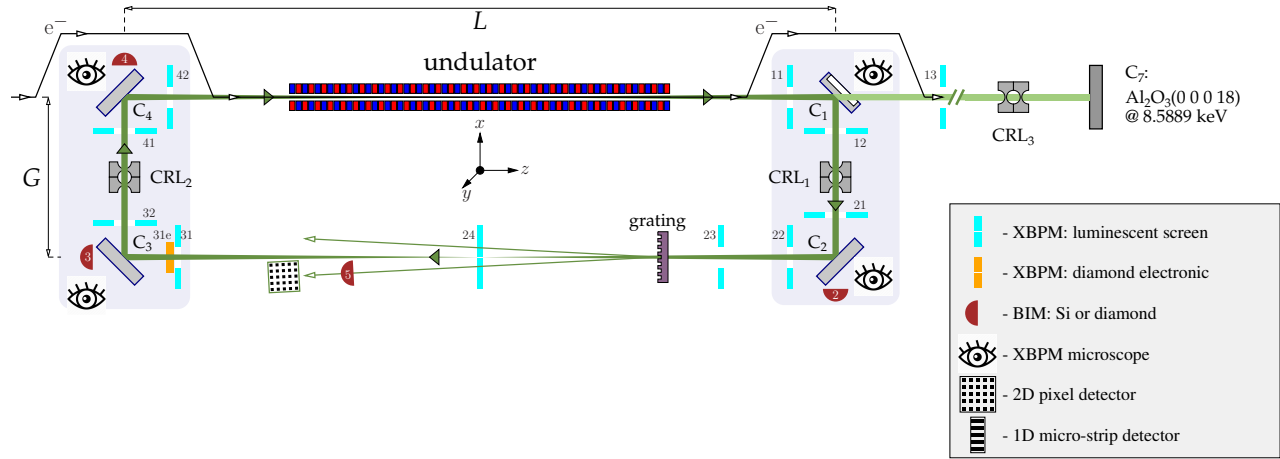


Figure 6.20: CBXFEL x-ray cavity with Bragg backreflecting Al_2O_3 crystal and CRL_3 installed in an experimental station for the alignment of XBMP_{42} onto the undulator axis.

- The luminescent screens with holes are used for initial localization of the x-rays reflected from each crystal, while XBPM_{24} and XBPM_{31e} are used for fine x-ray beam alignment.
- In addition to XBPM_{22} , XBPM_{23} is installed at a distance of $\simeq 2 - 3$ m downstream of C_2 for a more accurate angular alignment of C_2 with a purpose of better pointing the x-ray beam on to XBPM_{31} featuring a field of view limited to $10 \times 10 \text{ mm}^2$.
- Beam intensity monitors BIM_2 , BIM_3 and BIM_4 (which are Si PIN diodes) are installed behind the crystals to control crystals' angular positions of the peak reflectivity.
- ns-Resolution BIM_1 , BIM_5 and XBPM_{31e} (all diamond-based detectors) are to measure ring down and gain in the cavity.
- 2D-Alignment is finalized when all the multiply-reflected beams overlap on the XBPM_{24} installed in the symmetry point with the smallest waist size. This is verified not only by the $30\text{-}\mu\text{m}$ -thin boron-doped diamond luminescent screen XBPM_{24} (no hole), but also by a $30\text{-}\mu\text{m}$ -thin diamond quadrant electronic XBPM_{31e} (no hole). Both monitors will allow for better than $5\text{-}\mu\text{m}$ overlap and better than 10-nrad angular accuracy of alignment and stability.
- 1D-Alignment is finalized when the round-trip time of x-rays matches the time interval between electron bunches and as a consequence the XFEL gain is observed.

In more detail, we envision the alignment procedure following the steps listed below.

1. X-rays are sequentially reflected from the crystals. The crystal positions, tilts and Bragg angles of the 1st and of the next crystals are corrected (δ -angle correction as in Fig. 6.21) to guide x-rays through XBPMs.
2. Because the undulator and reverse lines are pre-aligned parallel to each other to a few μrad accuracy, achieving Bragg reflection from C_3 should result in a dramatic reduction of the angular δ -error to the μrad level.
3. When the alignment of C_1 , C_2 , and C_3 is finalized (with a few- μrad accuracy), next is to ensure coarse alignment of C_4 using XBMP_{42} , in the first step, and then to get the C_4 -reflected beam onto XBPM_{12} or/and D_2 via Bragg reflection from C_1 by using fine 2D angular and 1D linear scans of C_4 .

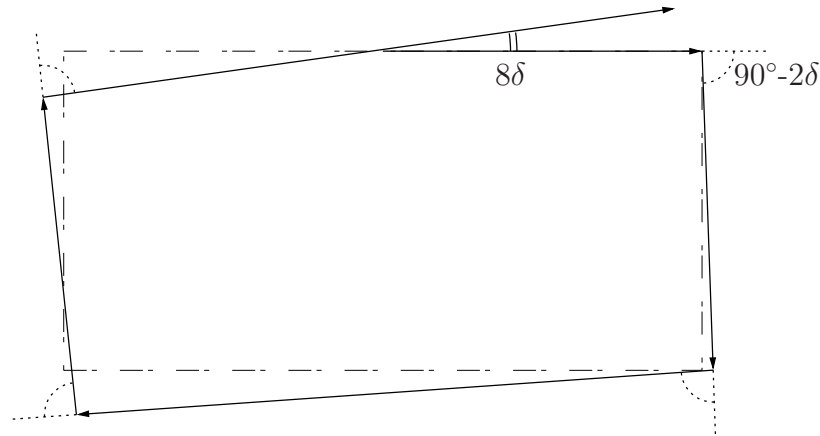


Figure 6.21: Typical miss-aligned trajectory of x-rays due to an initial angular error δ in the pitch angle of crystal C_1 , which amplifies to a 8δ misalignment after the round trip. The picture is simplified to a 2D case.

4. The round trip beam and the direct beam are most probably do not overlap immediately on XBPM₂₄. By measuring the deviation of the beams in the horizontal and vertical planes δ -error can be determined and further corrected (see 8δ -angular deviation in the horizontal plane in Fig. 6.21).
5. Change roll/tilt angles and positions of C_2 and/or C_3 and/or C_4 to place the multiple reflected beams into horizontal scattering plane (all multiple beams are on a horizontal line).
6. Change the pitch (Bragg) angles on all diamond crystals by the same amount and linear position of one crystal to have the multiply reflected beams overlap horizontally.
7. When the multiply-reflected beams overlap, proceed to tuning the round-trip length by translation of a pair of crystals and XBPMs in one branch until the XFEL gain is observed for the second pulse.

6.4.7 Mechanical System

As shown in Fig. 6.22 and described in Table 6.14, the mechanical system for the rectangular x-ray cavity of the CBXFEL at LCLS-II includes four sets of diamond crystal holders (C_1 , C_2 , C_3 , and C_4) with nanopositioning stages in UHV chambers. These nanopositioning stages and vacuum chambers are grouped into two crystal stations (stations A and B), and five diagnostic stations (stations C, D, E, F, and G). Each of the crystal stations shall be integrated with their associated chicane magnets and vacuum systems on the same girder to meet the requirement for LCLS-II e-beam-based alignment operation. The CBXFEL mechanical system also includes a vacuum pipe system as the cavity's X-ray return path. The X-ray diagnostic stations C, D, and E are located in the X-ray return path and its extension line. The X-ray/electron beam diagnostic station F is located in the LCLS-II experimental station. The X-ray diagnostic station G is located in the LCLS-II experimental station. Since it may not be in the same cavity vacuum system, the X-ray diagnostic station G will be designed separately.

There are three key functional requirements for the design of the mechanical system:

1. The system needs to meet all of the safety requirements for the operation integrated with the LCLS-II XFEL facility. Especially, the LCLS-II personnel safety interlock system must be in-

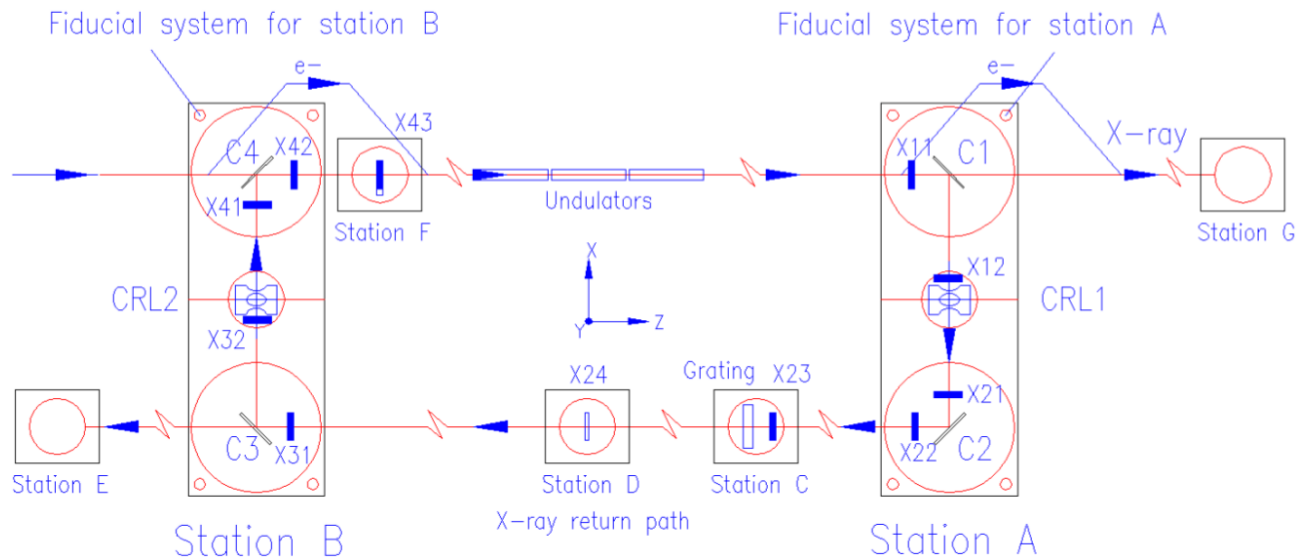


Figure 6.22: Schematic of the mechanical system for CBXFEL.

Cavity length adjustment	Total length	Uncertainty	Adjustment range	Resolution
Cavity total length	65.3 m	~ 33 micron	8 mm	50 nm
(C4 to C1) + (C2 to C3)	64 m	~ 29 micron	4 mm	50 nm
(C1 to C2) + (C3 to C4)	1.3 m	~ 4 micron	4 mm	50 nm

Table 6.14: Basic motion control requirements for CBXFEL mechanical system.

egrated with the cavity opto-mechanical system to prevent any unsafe radiation conditions during the system commissioning and operation.

2. The system shall support all of the nanopositioning requirements listed in other sections of this document to perform the cavity alignment process and keep the system stability for a successful cavity-based x-ray FEL experiment.
3. The system shall meet the LCLS-II vacuum requirements, be compatible with the chicane magnet system, and prevent any possible interference to the operation of the LCLS-II XFEL user facility.

6.4.7.1 Laser Interferometer

A customized commercial multichannel laser interferometer system shall be integrated as a part of the opto-mechanical system to monitor the cavity total length and XBPM locations during the system installation, commissioning and operation processes. With the laser interferometer's real-time measurements, the nanopositioning stages shall be able to compensate the thermal drifting of the mechanical system with a closed-loop feedback control. The laser interferometer system shall meet the following functional requirements:

- The laser interferometer system shall operate as an absolute distance measurement system, so that the measurement will not be disturbed with an accidental laser beam interruption, making the system more robust and reliable for operation.

- The laser interferometer system shall have a compact UHV-compatible fiber-optics front-end with a 2D flexure alignment holder compatible with the cavity nanopositioning stages.
- The laser interferometer system shall be operational under the radiation condition inside the CBXFEL cavity system with a reasonable life time.
- The laser interferometer system shall have a maximum measuring range larger than 32 meters with measurement uncertainty better than 0.4 micron/m.

6.4.7.2 Capacitive Sensor

Commercial miniaturized capacitive sensors are applied in the CBXFEL mechanical system to provide repeatable absolute measurement in a short distance to ensure the traceability of the metrology structure during the CBXFEL mechanical system assembly, installation, commissioning and operation processes. The capacitive sensors shall meet following functional requirements:

- The miniaturized capacitive sensors system shall be UHV compatible and be fitted with the cavity nanopositioning stages.
- The miniaturized capacitive sensors system shall be operational under the radiation condition inside the CBXFEL cavity system with a reasonable life time.
- The miniaturized capacitive sensor system shall have a maximum measuring range equal to or larger than 0.5 millimeters with measurement resolution better than 20 nm.

6.4.7.3 Vacuum System

The LCLS-II undulator segment vacuum chamber needs to be operated at a pressure better than 10^{-6} Torr in order to minimize bremsstrahlung and emittance growth. To achieve this, ion pumps need to be integrated with the CBXFEL vacuum chambers for the opto-mechanical system. Similar to the design of the LCLS-I and LCLS-II self-seeding monochromators, the vacuum system of the CBXFEL opto-mechanical system shall meet following functional requirements:

- The design of vacuum system shall have highest priority on the operation reliability and maintainability to minimize any possible interference to the operations of the LCLS-II XFEL user facility.
- All-metal manual isolation valves and welded bellows are the vacuum interfaces for the CBXFEL to the LCLS-II vacuum system.
- Vacuum feedthroughs and viewports are located according to the physical requirements for X-ray crystal optics and beam position monitors.
- Since the vacuum enclosures are housing for nanopositioning stages with precision metrology reference frames, special designs are needed to ensure its thermal and structural dynamical stability.

6.4.7.4 Metrology Reference frame and Base

Each of the crystal stations shall have an Invar base with global survey/alignment fiducial holes outside the vacuum. Metrology reference frames are established inside the vacuum enclosure to mount the laser interferometer's fiber-optics frontends and the capacitive sensor's sensing heads.

6.4.7.4-1 *Reference Base Installation Accuracy*

Using a laser-tracker system (such as Leica's TM MI-AT960 laser tracker), installation accuracy of the reference base is expected to be around ± 130 micron over the 32-meter range, with ± 1 micro-rad angular resolution in ~ 1 meter range [26]. A set of manual adjustment mechanisms is designed as an interface between each crystal station reference base and the girder system of the associated chicane magnets.

6.4.7.4-2 *The Positioning Transition Uncertainty between Reference Base and Frame*

The positioning transition uncertainty between the reference base and frame shall be better than 3 microns over the full length of the crystal station measured with a typical coordinate measuring machine (CMM) (such as Mitutoyo Crysta Apex S9106).

6.4.7.5 **Nanopositioning Stages for X-ray Optics and XBPMs Motion Control**

As shown in Fig. 6.22, three types of nanopositioning stage groups are designed for the CBXFEL opto-mechanical system:

1. Stage group for diamond crystal initial alignment, cavity fine turning, and total retrieval from the X-ray path.
2. Stage group for X-ray beam position monitor alignment, operation, and total retrieval from the X-ray path.
3. Stage group for X-ray compound refractive lens alignment, operation, and total retrieval from the X-ray path.

There are common functional requirements for the three types of nanopositioning stage groups:

- The nanopositioning stages shall be UHV compatible.
- The nanopositioning stages shall meet the requirements to perform cavity alignment, fine tuning, and retrieval process and keep the system stability for a successful experiment.
- To minimize the heat consumption of the stages in a vacuum environment, all of the nanopositioning stages are driven by PZT-based motors or actuators.

6.4.7.5-1 *Nanopositioning Stages for Diamond Crystal Motion Control*

As shown in Fig. 6.23, the nanopositioning stage group for diamond crystal manipulation includes four precision flexure stages and three (or four, with an extra yaw adjustment stage) miniaturized PZT-motor-driven precision bearing stages. Fig. 6.24 shows a 3D model of the tip-tilting flexure stages for diamond crystal pitch and roll motion control. Basic motion control requirements (travel range and positioning resolution) are listed in Table 6.15.

The home position of each stage shall be measured by CMM during the final assembly process with 3 micron measurement uncertainty to the reference base global survey/alignment fiducial holes.

The home positions are traceable with the reading of the capacitive sensors and laser interferometers directly mounted on the invar reference frame. For several less-critical stages, they are traceable with grating encoders.

A diamond crystal holder is mounted on the top of the stage group. The holder is similar to the APS designed diamond crystal holder for European-XFEL self-seeding monochromator. A heater

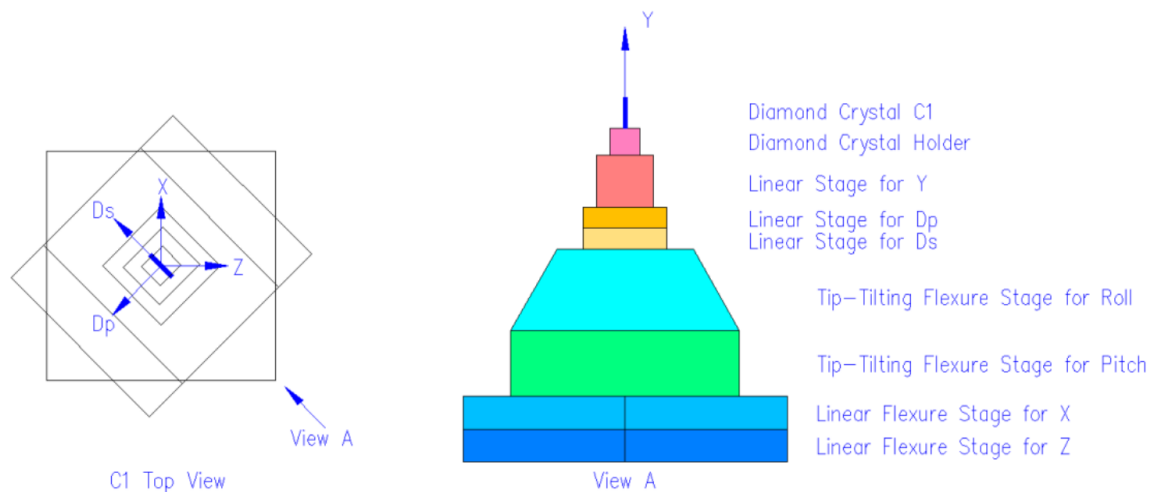


Figure 6.23: Schematic of the nanopositioning stage group for diamond crystal manipulation.

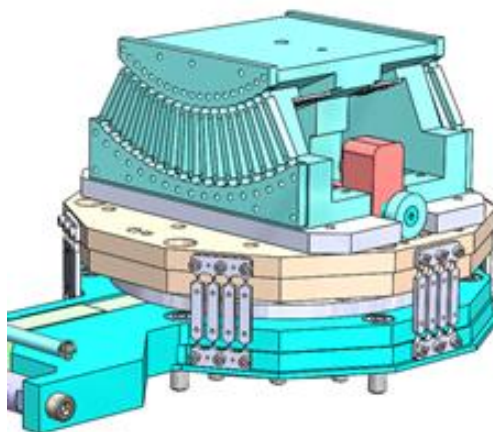


Figure 6.24: 3D model of the tip-tilting flexure stages for diamond crystal pitch and roll motion control.

Stage name	Travel range	Resolution
Linear flexure stage for Z (coarse)	1000 micron	50 nm
Linear flexure stage for Z (fine, optional)	15 micron	5 nm
Linear flexure stage for X (coarse)	1000 micron	50 nm
Linear flexure stage for X (fine, optional)	15 micron	5 nm
Tip-Tilting flexure stage for pitch (coarse)	26 mrad ($\sim 1.5^\circ$)	350 nrad
Tip-Tilting flexure stage for pitch (fine)	0.1 mrad	20 nrad
Tip-Tilting flexure stage for yaw (coarse)	26 mrad ($\sim 1.5^\circ$)	350 nrad
Tip-Tilting flexure stage for yaw (fine)	0.1 mrad	20 nrad
Linear stage for Ds	12 mm	50 nm
Linear stage for Dp	12 mm	50 nm
Linear stage for Y	12 mm	50 nm

Table 6.15: Basic motion control requirements for nanopositioning stage group for diamond crystal manipulation.

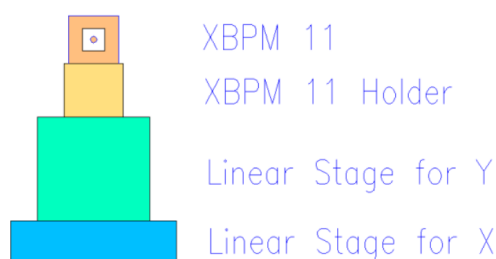


Figure 6.25: Schematic of the nanopositioning stage group for X-ray beam position monitor X11.

Stage name	Travel range	Resolution
Linear stage for Z	12 mm	50 nm
Linear stage for Y	12 mm	50 nm

Table 6.16: Basic motion control requirements for nanopositioning stage group for XBPM 12.

with thermostat shall be installed on the holder to keep an even temperature for all of the diamond crystals in the cavity system.

6.4.7.5-2 Nanopositioning Stages for X-ray beam position monitors

As shown in Fig. 6.25, the nanopositioning stage group for X-ray beam position monitors includes two miniaturized PZT-motor-driven precision bearing stages. Basic motion control requirements (travel range and positioning resolution) are listed in Table 6.16.

The home position of each stage shall be measured during the final assembly process using a CMM with 3-micron measurement uncertainty related to the reference base global survey/alignment fiducial holes.

The home positions are traceable with the reading of the capacitive sensors.

The same type of the stage group is used for X-ray diagnostic station C that is located in the middle of the X-ray return path for the X-ray wave-front interferometer grating manipulation.

A holder for the XBPM is mounted on the top of the stage group.

6.4.7.5-3 Nanopositioning Stages for X-ray compound refractive lenses

As shown in Fig. 6.26, the nanopositioning stage group for X-ray compound refractive lenses includes two larger PZT-motor-driven precision bearing stages. Basic motion control requirements (travel range and positioning resolution) are listed in Table 6.17.

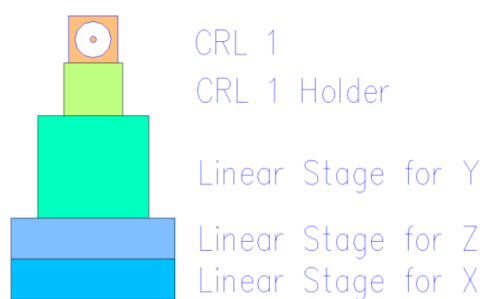


Figure 6.26: Schematic of the nanopositioning stage group for X-ray compound refractive lens CRL 1.

Stage name	Travel range	Resolution
Linear stage for X	12 mm	50 nm
Linear stage for Z (optional)	12 mm	50 nm
Linear stage for Y	12 mm	50 nm

Table 6.17: Basic motion control requirements for nanopositioning stage group for CRL 1.

Home position of each stage shall be measured by CMM during the final assembly process with 3 micron measurement uncertainty related to the reference base global survey/alignment fiducial holes.

The home positions are traceable with the reading of the capacitive sensors.

A holder for the X-ray compound refractive lenses is mounted on the top of the stage group.

6.4.7.5-4 *Interface to the CBXFEL control system*

Drivers and controllers for PZT-motors, actuators, capacitive sensors, and laser interferometer shall be supplied by original hardware manufacturers with basic operation software.

6.5 Electron/photon Beam Overlap Diagnostics

The electron beam and the x-ray beam must have sufficient overlap in space and time as they both travel along the undulators beam axis to maximize their interactions in order to achieve FEL gain for both XRAFEL and XFEL studies. In the current system layout, we can separate the requirements into those for the transverse and those for the longitudinal directions.

6.5.1 Transverse overlap

For transverse overlap, as indicated in Figure 6.22, spatial diagnostics needs to be installed at the two chicane locations that can accurately measure the electron and x-ray positions separately as the other one is turned off. It is required that the two separate measurements can be accurately referenced to each other, such that the average relative position of the x-ray and electron beams be measured with better than 10% of the beam size or $\approx 5 \mu\text{m}$ accuracy. This assumes also that the electron beam trajectory have deviation from a straight line by less than $5 \mu\text{m}$. This shall be evaluated and guaranteed by using the electron BPMs in between the undulators.

In addition, the spatial diagnostics shall provide beam transverse size information in order to assess the quality and size similarity of the electron and x-ray beams at the input and output end of the undulators with a resolution better than $20 \mu\text{m}$.

6.5.2 Longitudinal overlap

The temporal overlap requirement between the electron bunch and the recirculated photon pulse is driven by the bunch and pulse lengths. For XFEL, the electron bunch length will be longer than the transform limit of the diamond (400) reflection, and the temporal overlap requirement will be dominated by the desired electron bunch length of ≈ 300 fs. For XRAFEL, the desired electron bunch length of 50 fs (FW) is similar to the transform limit of the x-ray pulse length defined by the cavity bandwidth of ~ 70 meV which is ~ 30 fs. This will impose a more stringent requirement on longitudinal stability as discussed in section 6.4.2.1

We are current not foreseeing direct temporal overlap diagnostics in the time domain at the femtosecond level between the 2nd electron bunch and the x-ray pulse from the 1st electron bunch returned by the cavity. Temporal overlap will be established by the measurement of FEL gain as a function of cavity length while we have sufficient confidence about the spatial overlap between the returned x-ray beam and the 2nd electron bunch. After initial cavity length adjustment established by metrology down to $\pm 100 \mu\text{m}$ level, the temporal overlap requirement translates to angular crosstalk requirement of the delay adjustment (namely, the amount that the crystal angle changes as one adjusts its longitudinal position). At this stage, we set this requirement to be that the maximum allowed angular crosstalk shall be below 100 nrad over 3 times the cavity length confidence of $\pm 300 \mu\text{m}$.

6.6 Measurements

6.6.1 Ring-down

The ring-down experiments characterizes the performance of the x-ray optical cavity. It will give us a measure of the both the quality of cavity optical components and their respective alignment accuracy. Measurements can be performed with a single electron bunch mode. The decay of the intensity of the x-ray pulse trapped in the cavity will be measured. The intensity decay can be attributed to a variety of origins: less than 100% peak crystal Bragg reflectivity; accumulation of wavefront distortions due crystal Bragg plane errors; misalignment of the optical components; absorption losses in CRLs, x-ray diagnostics, and in residual gases in the cavity; finite spectral and angular acceptance of the cavity crystals; etc. The intensity of the sequence of x-ray pulses within the cavity is an exponential function of the number of round trips with one or several time constants, characteristic of the cavity losses. There are several ways of performing the ring-down measurements, which may provide different information on the cavity losses.

6.6.1.1 Intra-cavity measurement

The time dependence of the x-ray pulses propagating within the cavity can be measured with the intra-cavity x-ray intensity diagnostics, for example, a transparent detector, which in our case can be diamond quadrant XBPM_{31e} (in the beam intensity monitor mode) see Fig. 6.17. Leakage of x-rays through crystals C_2 , C_3 , and C_4 measured by beam intensity monitors BIM₂, BIM₂, and BIM₂, respectively provides related information. This measurement can be performed independent of the cavity beam outcoupling. When one of the output coupling schemes (thin crystal C_1 or diamond transmission grating) is activated, the ring-down measurement is expected to reveal a faster decay constant due to the outcoupling.

Due to varying crystal reflectivity as a function of photon energy and angle, even within the narrow cavity bandwidth and the small divergence of the FEL beam, as illustrated in spectral profiles of cavity reflectivity in Figs. 6.9(a)-(c), the measured ring-down time constant will reflect the averaged value of the crystal reflectivity, rather than its peak value. However, having access to the peak reflectivity value is the most important for the characterization of the cavity in the context of XFEL. For this purpose it is valuable to perform higher energy resolution ($\simeq 10 - 20 \text{ meV}$) measurement at the peak reflectivity of the cavity crystals, as was performed in the cavity ring-down experiment [27]. This can be achieved by inserting a monochromator in one of the intra-cavity diagnostic lines, or downstream on the out-coupled beam which will be discuss next.

6.6.1.2 Extra-cavity measurement

The x-ray monochromator for the ring-down measurements can be installed downstream in the experimental hall, looking on x-rays out-coupled through thin crystal C_1 . We will use a double crystal Si monochromator in the nondispersive setting set into the (337) Bragg reflection with a bandwidth of 17 meV, presented by crystals C_5 – C_6 in Fig. 6.17. Similarly, Si crystals in the (660) Bragg reflection can be used, providing a monochromator with a slightly larger bandwidth of 20-meV, but higher throughput. Time dependence will be recorded with a pulse resolving x-ray detector BIM₁.

6.6.2 Two pass gain

Two-pass gain measurements allow for the investigation of crucial aspects related to CBXFEL physics using a pair of electron bunches. They are critical for demonstrating cavity tolerance and stability requirements for both the high and low gain cavity FEL schemes. This measurement begins with the first electron bunch producing spontaneous x-ray radiation in the undulator line. The first electron bunch is then sent to the dump while the x-rays are monochromatized and returned to the undulator entrance by the x-ray cavity. Once the returned x-rays overlap with the second fresh electron bunch, which then generates additional radiation in a seeded FEL process. To achieve FEL gain requires that the trajectories of the returned x-rays and the second electron bunch overlap both spatially and temporally, which in turn means that the transverse position and angle of the second electron beam matches that of the x-rays, and that the time delay between the two electron bunches equals the cavity transit time.

This section provides an estimate on the number of photons for both the XRA FEL (high-gain) and XFEL (low-gain) schemes for the first and second pass amplification. These numbers are obtained through detailed numerical particle FEL and optical propagation simulations. The simulations are driven by the requirements on the electron bunch parameters (section 6.1), the undulator parameters (section ??), and the cavity parameters (section 6.4). The performance of the system will be measured by the diagnostics outlined in section 6.4.5.

6.6.2.1 XRA FEL

Roughly 50 independent, 2-pass, time-dependent FEL and cavity simulations were performed under the assumption that the four cavity mirrors have independent angular errors that are normally distributed. Five scenarios were considered where the independent angular errors on each of the cavity mirrors had RMS fluctuations of $\sigma_m = 0, 100, 200, 300, 400$ nrad (also, see section 6.4.2.1 for more detail). Only cavity mirror errors were considered here. The two electron bunches are assumed to be perfectly aligned in trajectory and perfectly spaced according to the cavity roundtrip time. The $\sigma_m = 0$ nrad dataset indicates an aligned cavity and acts as the basis of comparison for the performance of the system under the various error scenarios presented here.

Table 6.18 shows the results for the number of photons produced in the first and second pass. In addition, the number of photons within the cavity bandwidth are also presented along with the average 2-pass gain.

6.6.2.2 XFEL

A similar set of simulations has also been done for the low-gain (XFEL) parameters as was just described, and the results are gathered in Table 6.19. As seen in the Table, for the XFEL parameters we expect the number of photons generated in the first pass to be approximately equal to that of the second pass, $N_1 \approx N_2$, since the radiation is dominated by spontaneous emission over a broad

Mirror error	N_1	N_1^{BW}	N_2	N_2^{BW}	$\langle N_2^{BW}/N_1^{BW} \rangle$
$\sigma_m = 0$	$200(1.8) \times 10^6$	$9.2(8.1) \times 10^5$	$24(2.7) \times 10^7$	$5.5(3.9) \times 10^7$	86 (76)
$\sigma_m = 100$ nrad	$200(2.1) \times 10^6$	$7.3(5.1) \times 10^5$	$23(1.8) \times 10^7$	$4.5(3.3) \times 10^7$	88 (101)
$\sigma_m = 200$ nrad	$200(1.8) \times 10^6$	$7.4(5.8) \times 10^5$	$22(1.9) \times 10^7$	$3.6(3.2) \times 10^7$	63 (66)
$\sigma_m = 300$ nrad	$200(1.5) \times 10^6$	$7.7(6.5) \times 10^5$	$22(1.7) \times 10^7$	$3.7(3.2) \times 10^7$	62 (49)
$\sigma_m = 400$ nrad	$200(1.7) \times 10^6$	$7.3(5.3) \times 10^5$	$22(1.2) \times 10^7$	$2.5(2.2) \times 10^7$	52 (62)

Table 6.18: High gain photon numbers. $N_{1(2)}$: Number of photons in the first(second) pass. $N_{1(2)}^{BW}$: Number of photon in the first(second) pass in the cavity bandwidth. The numbers in parentheses in each cell indicates the RMS fluctuation.

spectrum. On the other hand, amplification of the radiation within the narrow bandwidth of the Bragg crystals results in an increase in N_2^{BW} by a factor of 2 to 2.4, depending upon the CRL focal length chosen. This ratio does not decrease when we include random variations in the crystal angles whose RMS is $\sigma_m = 50$ nrad, consistent with what was shown in Sec. 6.4.2.2. Finally, we note that the expected photon output in the narrow bandwidth for the XFEL, $N_2 \approx 1.5 \times 10^5$, is about a factor of 400 less than that listed for the XRA FEL parameters, so that the detection system must be able to handle a dynamic range that is better than a factor of 10^3 .

Mirror parameters	N_1	N_1^{BW}	N_2	N_2^{BW}	$\langle N_2^{BW}/N_1^{BW} \rangle$
$\sigma_m = 0, f = 14.18$ m	$2853(6) \times 10^4$	$6.9(0.6) \times 10^4$	$2865(10) \times 10^4$	$16(4) \times 10^4$	2.4(0.5)
$\sigma_m = 0, f = 28.36$ m	$2853(6) \times 10^4$	$6.9(0.6) \times 10^4$	$2861(8) \times 10^4$	$13(2) \times 10^4$	2.0(0.3)
$\sigma_m = 50, f = 14.18$ m	$2853(6) \times 10^4$	$6.9(0.6) \times 10^4$	$2865(8) \times 10^4$	$16(3) \times 10^4$	2.4(0.4)
$\sigma_m = 50, f = 28.36$ m	$2853(6) \times 10^4$	$6.9(0.6) \times 10^4$	$2863(8) \times 10^4$	$14(2) \times 10^4$	2.0(0.4)

Table 6.19: Photon numbers for low-gain XFEL. N_1 is the total photon number and N_1^{BW} is the number of photons in the crystal bandwidth after the first pass, which are the same for all simulations. The number of photons after the second pass N_2 and the number in the crystal bandwidth N_2^{BW} vary little with mirror errors on the 50 nrad level and with the focal length choice. Numbers in parentheses indicates the RMS fluctuation.

6.7 Controls

The overall controls approach is built upon each modular sub-system delivering integrated motion, power and feedback controls that are compatible and functional with LCLS-II electrical hardware and software interface. The controls and software at the system level will be a separate effort and integrate all subsystems to LCLS-II. The organization and ownership of the subsystems are detailed in Chapter 4. A typical example for SXRSS integrated in LCLS-II control system is shown in Fig. 6.27.

General guidelines for design of subsystems to be compatible with LCLS-II are listed below:

1. For macro-scale e.g. millimeter high precision motion controls, SLAC controls utilizes Delta Tau PowerPMAC motion controller to control either EtherCAT or Ster/Direction type drives. Additionally, the PowerPMAC controller is used with Renishaw Resolute BiSS-C absolute encoder for high resolution position feedback. PowerPMAC controller is also utilized on HXR undulators to read full-gap absolute encoders. Any future projects that are integrated into the undulator beamline are recommended to use PowerPMAC controllers.
2. For piezo-actuators utilized in ultra-fine precision motion controls e.g. micro- and nano- level

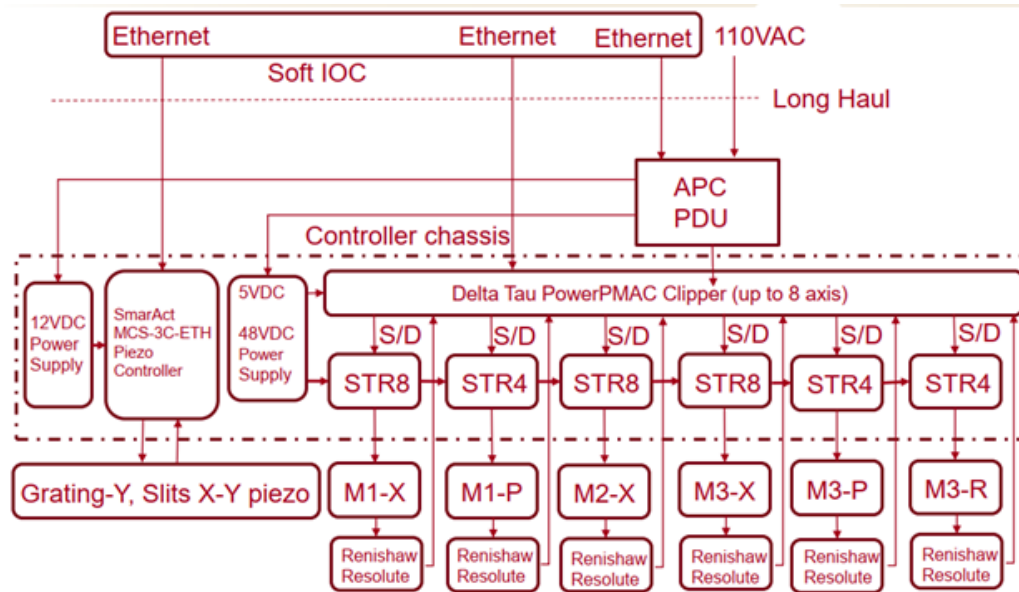


Figure 6.27: Exampe of SXRSS integrated in LCLS-II Controls System.

motion control, manufacturer-supplied motion controllers can be considered. SmarAct is one of the preferred manufacturers for the piezo actuator linear stages used in LCLS-II HXR and SXR optical chambers.

In order to minimize risk to the LCLS-II user facility, interface controls will be mutually agreed between subsystems and overall system owners at the start of the Preliminary Design phase. Additionally, all electrical and motion control components will be mutually agreed/approved between subsystem owners and SLAC's EED Controls prior to design finalization and procurement.

6.8 Machine Protection Systems

The electron beam may strike the inserted optics in cells 13 and 21 if the chicane power supplies trip off or are set too low. To protect the optical components against this occurrence, both of the upstream and downstream chicane excitation currents should be monitored by the machine protection system (MPS) in order to shut off the electron beam via the vertical bend abort kicker in the linac to undulator transport line as fast as possible (within < 3 pulses). Furthermore, the local HXR undulator beam loss monitors, which are already interlocked to the MPS, will also detect an elevated electron bunch charge loss and redundantly trip off the electron beam. If either or both of the optics chambers are inserted, the electron beam should be disabled *unless* the pre-undulator dump tune-up dump is inserted *or* the chicanes are powered at or near their normal operating ranges *and* the electron beam energy is at or near the normal operating range.

6.9 Other global and safety requirements

ANL delivered optical components and chambers must mechanically fit the SLAC chicane magnet assembly. The SLAC X-ray beam diagnostics and chambers must be mechanically compatible with the ANL delivered return vacuum pipe. The ANL delivered return vacuum pipe is envisioned to have an alignment system that is compatible with SLAC alignment engineering.

The design and operation of each subsystem are interdependent. Therefore, management of interface control specifications of the subsystems is critical to the success of this project. Each subsystem is also expected to be validated to be fully functional before installation and integration at SLAC due to the logistical challenge associated with fixing ANL subsystems remotely.

All electrical components must comply with all applicable SLAC electrical safety requirements.

All mechanical systems must comply with all applicable SLAC earthquake and mechanical safety requirements.

Chapter 7

End Notes

Bibliography

- [1] A. Snigirev, V. Kohn, I. Snigireva, and B. Lengeler. A compound refractive lens for focusing high-energy x-rays. *Nature*, 384:49–51, 1996.
- [2] Yu. V. Shvyd'ko, S. Stoupin, V. Blank, and S. Terentyev. Near 100% Bragg reflectivity of x-rays. *Nature Photonics*, 5:539–542, 2011.
- [3] Tomasz Kolodziej, Preeti Vodnala, Sergey Terentyev, Vladimir Blank, and Yuri Shvyd'ko. Diamond drumhead crystals for X-ray optics applications. *Journal of Applied Crystallography*, 49(4):1240–1244, Aug 2016.
- [4] R C Burns, A I Chumakov, S H Connell, D Dube, H P Godfried, J O Hansen, J Härtwig, J Hoszowska, F Masiello, L Mkhonza, M Rebak, A Rommevaux, R Setshedi, and P Van Vaerenbergh. HPHT growth and x-ray characterization of high-quality type IIa diamond. *J. Phys.: Condensed Matter*, 21:364224(14pp), 2009.
- [5] S. N. Polyakov, V. N. Denisov, N. V. Kuzmin, M. S. Kuznetsov, S. Yu. Martyushov, S. A. Nosukhin, S. A. Terentiev, and V. D. Blank. Characterization of top-quality type IIA synthetic diamonds for new x-ray optics. *Diamond and Related Materials*, 20(5-6):726–728, 2011.
- [6] H. Sumiya and K. Tamasaku. Large defect-free synthetic type IIA diamond crystals synthesized via high pressure and high temperature. *Japn. J. Appl. Phys.*, 51:090102, 2012.
- [7] Yuri Shvyd'ko, Vladimir Blank, and Sergey Terentyev. Diamond x-ray optics: Transparent, resilient, high-resolution, and wavefront preserving. *MRS Bulletin*, 62(6):437–444, 2017.
- [8] B. Lengeler, C. Schroer, J. Tümmler, B. Benner, M. Richwin, A. Snigirev, I. Snigireva, and M. Drakopoulos. Imaging by parabolic refractive lenses in the hard x-ray range. *J. Synchrotron Radiation*, 6:1153, 1999.
- [9] Stanislav Stoupin, Yuri Shvyd'ko, Emil Trakhtenberg, Zunping Liu, Keenan Lang, Xianrong Huang, Michael Wiczorek, Elina Kasman, John Hammonds, Albert Macrander, and Lahsen Assoufid. Sequential x-ray diffraction topography at 1-BM x-ray optics testing beamline at the Advanced Photon Source. *AIP Conf. Proc.*, 1471:050020, 2016.
- [10] Tomasz Kolodziej, Stanislav Stoupin, Walan Grizolli, Jacek Krzywinski, Xianbo Shi, Kwang-Je Kim, Jun Qian, Lahsen Assoufid, and Yuri Shvyd'ko. Efficiency and coherence preservation studies of Be refractive lenses for XFEL application. *Journal of Synchrotron Radiation*, 25(2):354–360, Mar 2018.
- [11] Kwang-Je Kim, Yuri Shvyd'ko, and Sven Reiche. A proposal for an x-ray free-electron laser oscillator with an energy-recovery linac. *Phys. Rev. Lett.*, 100(24):244802, Jun 2008.

- [12] Kwang-Je Kim and Yuri V. Shvyd'ko. Tunable optical cavity for an x-ray free-electron-laser oscillator. *Phys. Rev. ST Accel. Beams*, 12(3):030703, Mar 2009.
- [13] Yu. Shvyd'ko. Feasibility of x-ray cavities for free electron laser oscillators. *Beam Dynamics Newsletter*, 60:68–83, April 2013. International Committee for Future Accelerators.
- [14] Yuri Shvyd'ko and Ryan Lindberg. Spatiotemporal response of crystals in x-ray Bragg diffraction. *Phys. Rev. ST Accel. Beams*, 15:100702, Oct 2012.
- [15] A. Authier. *Dynamical Theory of X-Ray Diffraction*, volume 11 of *IUCr Monographs on Crystallography*. Oxford University Press, Oxford, New York, 2001.
- [16] Yuri Shvyd'ko. Output coupling from x-ray free-electron laser cavities with intracavity beam splitters. *Phys. Rev. Accel. Beams*, 22:100703, Oct 2019.
- [17] M. Makita, P. Karvinen, D. Zhu, P. N. Juranic, J. Grünert, S. Cartier, J. H. Jungmann-Smith, H. T. Lemke, A. Mozzanica, S. Nelson, L. Patthey, M. Sikorski, S. Song, Y. Feng, and C. David. High-resolution single-shot spectral monitoring of hard x-ray free-electron laser radiation. *Optica*, 2(10):912–916, Oct 2015.
- [18] Tetsuo Katayama, Shigeki Owada, Tadashi Togashi, Kanade Ogawa, Petri Karvinen, Ismo Vartiainen, Anni Eronen, Christian David, Takahiro Sato, Kyo Nakajima, Yasumasa Joti, Hirokatsu Yumoto, Haruhiko Ohashi, and Makina Yabashi. A beam branching method for timing and spectral characterization of hard x-ray free-electron lasers. *Structural Dynamics*, 3(3):034301, 2016.
- [19] Kenan Li, Yanwei Liu, Matthew Seaberg, Matthieu Chollet, Thomas Weiss, and Anne Sakdinawat. Wavefront preserving and high efficiency diamond grating beam splitter for x-ray free electron laser. *Optics Express*.
- [20] Makina Yabashi, Jerome B. Hastings, Max S. Zolotarev, Hidekazu Mimura, Hirokatsu Yumoto, Satoshi Matsuyama, Kazuto Yamauchi, and Tetsuya Ishikawa. Single-shot spectrometry for x-ray free-electron lasers. *Phys. Rev. Lett.*, 97:084802, Aug 2006.
- [21] Diling Zhu, Marco Cammarata, Jan M. Feldkamp, David M. Fritz, Jerome B. Hastings, Soohyeon Lee, Henrik T. Lemke, Aymeric Robert, James L. Turner, and Yiping Feng. A single-shot transmissive spectrometer for hard x-ray free electron lasers. *Appl. Phys. Lett.*, 101:034103, 2012.
- [22] Yuri Shvyd'ko, Stanislav Stoupin, Kiran Mundboth, and Jungho Kim. Hard-x-ray spectrographs with resolution beyond 100 μev . *Phys. Rev. A*, 87:043835, Apr 2013.
- [23] Yuri Shvyd'ko. Theory of angular-dispersive, imaging hard-x-ray spectrographs. *Phys. Rev. A*, 91:053817, May 2015.
- [24] Aleksandr I. Chumakov, Yuri Shvyd'ko, Ilya Sergueev, Dimitrios Bessas, and Rudolf Ruffer. Hard-x-ray spectroscopy with a spectrographic approach. *Phys. Rev. Lett.*, 123:097402, Aug 2019.
- [25] J. Zhang, M. Andrä, R. Barten, A. Bergamaschi, M. Brückner, R. Dinapoli, E. Fröjd, D. Greiffenberg, C. Lopez-Cuenca, D. Mezza, A. Mozzanica, M. Ramilli, S. Redford, M. Ruat, C. Ruder, B. Schmitt, X. Shi, D. Thattil, G. Tinti, M. Turcato, and S. Vetter. Towards Gotthard-II: development of a silicon microstrip detector for the european x-ray free-electron laser. *Journal of Instrumentation*, 13(01):P01025, 2018.
- [26] W. Jansma. Private communication with D. Shu. 2019.

- [27] Yu. V. Shvyd'ko, M. Lerche, H.-C. Wille, E. Gerdau, E. E. Alp, M. Lucht, H. D. Rüter, and R. Khachatryan. X-ray interferometry with micro-electronvolt resolution. *Phys. Rev. Lett.*, 90:013904, 2003.